Depth-dependent controls on structure, reactivation and geomorphology of the active Thyolo border fault, Malawi rift

Luke N. J. Wedmore[1], Jack N Williams[2], Juliet Biggs[1], Åke Fagereng[2], Felix Mphepo[3], Zuze Dulanya[4], James Willoughby[1], Hassan Mdala[3], Byron Adams[1]*

[1]*School of Earth Sciences, University of Bristol, UK*

[2]*School of Earth and Ocean Sciences, Cardiff University, UK*

[3]*Geological Survey Department, Mzuzu Regional Office, Mzuzu, Malawi*

[4]*Geography and Earth Sciences Department, University of Malawi, Zomba, Malawi*

**Corresponding author: luke.wedmore@bristol.ac.uk*

Keywords

High-resolution topography, pre-existing structures, normal faults, rifts, border fault, damage zone

Highlights

- The Thyolo fault, Malawi, is a rift border fault with a polyphase tectonic history
- Satellite and field data confirm recent activity on an 18.6 ± 7.7 m high scarp
- The fault is segmented, but scarp height sectors do not align with geometry changes
- The fault damage zone is 15-180 m wide with an unusually narrow 0.7 m fault core
- The Thyolo fault may be reactivating a deep ductile zone along a terrane boundary

Abstract

We present new observations of the geometry and pattern of fault growth from the Thyolo fault, an 85 km long border fault in the southern Malawi Rift, from high-resolution topography and field observations. The rift has a polyphase tectonic history and the Thyolo fault is located towards the edge of the Proterozoic Unango Terrane. Recent activity is demonstrated by an 18.6 ± 7.7 m high fault scarp. Different patterns of segmentation are indicated by fault geometry and fault displacement profiles: two substantial reductions in scarp height do not coincide with surface geometry changes. The surface scarp is divided into two geometrically defined overlapping sections, which are joined by a ~5 km long, fault perpendicular scarp. The scarp height in this linking section is similar to the bounding sections, yet the river drainage network and sediment depocenter distribution is not typical of relay zones. Microstructural and compositional analyses show a 15-180 m thick damage zone with an unusually narrow 0.7 m thick fault core. These features can be explained if the fault exploits weak ductile zones at depth, such as heterogeneity associated with the Unango Terrane boundary, while near surface geometry is controlled by well-oriented, frictionally strong but low-cohesion shallow structures.

1. Introduction

Narrow amagmatic rifts (sensu Buck, 1991), are typically characterised by a ≤100 km wide graben or half graben where the greatest cumulative displacement is accommodated on large offset normal fault systems, known as rift border faults, that bound a region of distributed but relatively small displacement brittle deformation (Ebinger, 1989; Gawthorpe and Leeder, 2000; Muirhead et al., 2019). These basin-bounding faults are thought to be most active prior to any magmatic influence on rifting (Ebinger, 2005; Muirhead et al., 2019), have a distinctive impact on basin geomorphology (Leeder and Gawthorpe, 1987; Gawthorpe and Leeder, 2000) and can accumulate sufficient displacement so that flexural bending induces intrabasin strain (Turcotte and Schubert, 2002). Furthermore, border faults can penetrate the

entire depth of the crust, and in East Africa are probably the source of some of the deep earthquakes within the ~40 km thick seismogenic layer (Lavayssière et al., 2019).

How faults grow from nucleation to crustal scale features is a long-standing topic of research (Cowie and Scholz, 1992b; Cowie, 1998; Walsh et al., 2002; Nicol et al., 2005; Worthington and Walsh, 2017; Rotevatn et al., 2019), and numerous studies have mapped fault trace geometry and measured displacement-length profiles to discuss the mechanism and timing of how long faults develop through segment initiation, growth, and linkage (Cowie and Scholz, 1992a, 1992b, 1992c; Scholz et al., 1993; Dawers et al., 1993; Dawers and Anders, 1995; Schlische et al., 1996; Walsh et al., 2003; Nicol et al., 2005, 2017; Giba et al., 2012; Rotevatn et al., 2018). Structural heterogeneities at segment boundaries that result from fault growth are thought to influence the propagation and termination of earthquake ruptures (Segall and Pollard, 1980; Zhang et al., 1991; Wesnousky, 2006, 2008), yet recent earthquakes (e.g. 2010 M_w7.2 El Mayor-Cucapah Earthquake, Mexico – Wei et al., 2011 and the 2016 M_w7.8 Kaikoura Earthquake, New Zealand – Hamling et al., 2017) have cut across multiple segment boundaries and thus it remains unclear how to best assess fault segmentation for seismic hazard purposes (DuRoss et al., 2016). Border faults are now generally thought to develop through the accumulation of displacement on fault segments that formed and linked during the early stages of rifting (Gawthorpe et al., 2003; Rotevatn et al., 2019; Muirhead et al., 2019); however, the effects of this linkage on the displacement profile and geometry of a fault is commonly long-lasting. Minima in fault displacement profiles and displacement anomalies are persistently observed at segment boundaries (Machette

et al., 1991; Gupta and Scholz, 2000; Mortimer et al., 2007, 2016) as are relay ramps, increased fault complexity, and changes in fault geometry (Leeder and Gawthorpe, 1987; Crone and Haller, 1991a; Peacock and Sanderson, 1991; Crider and Pollard, 1998; Fossen and Rotevatn, 2016; Hodge et al., 2018a). Thus, observations of fault segmentation provide a permanent record of processes that occurred during the formation and linkage of fault segments, and consequently they offer insights into the fundamental processes of fault growth and the controls on the limits of earthquake rupture propagation.

Rifts rarely initiate and grow in isotropic crust, and therefore it is important to understand the effect of pre-existing heterogeneities and structures on the growth and segmentation of faults. Structures, such as pre-existing lithospheric weaknesses, are often cited as the predominant control on rift geometry, the distribution of strain within rifts, and the oblique orientation of magmatic bodies, magmatic rift segments and faults relative to the regional minimum compressive stress (McConnell, 1967; Daly et al., 1989; Ebinger et al., 1997; Morley, 2010; Henstra et al., 2015; Robertson et al., 2016; Muirhead and Kattenhorn, 2018). At the scale of an individual fault, the effect of pre-existing fabrics on fault growth has been constrained using analogue models, where reactivated structures have been shown to affect the fault geometry, relay zone geometry and the distribution of basins (Bellahsen and Daniel, 2005; Henza et al., 2011). However, comparisons with real faults in a natural setting is often more difficult as it can be difficult to differentiate between contemporary and pre-rift heterogeneities that have similar geometries (Smith and Mosley, 1993; Holdsworth et al., 1997), especially using seismic

reflection and aeromagnetic surveys, which can only resolve features at scales >10 m.

Investigating the interactions between pre-existing fabrics and strain localisation on rift border faults also requires understanding the structure and mechanics of these faults. In general, as faults grow, they accumulate damage in the rocks surrounding the fault (Cowie and Scholz, 1992b; Caine et al., 1996; Shipton and Cowie, 2003). However, the structure of a rift border fault has only been described in a limited number of cases (Ord et al., 1988; Wheeler and Karson, 1989; Kristensen et al., 2016; Hollinsworth et al., 2019), with most models of normal fault structural evolution based on studies of small displacement (<100 m) faults within high porosity sedimentary rock (Shipton and Cowie, 2003; Childs et al., 2009; Torabi and Berg, 2011; Savage and Brodsky, 2011). Consequently, it remains unclear whether these models are applicable to large offset rift border faults where the footwall is composed of foliated crystalline metamorphic rocks.

In this paper, we analyse the Thyolo fault, the border fault of the Lower Shire Graben in southern Malawi (Figure 1). The fault is an ideal location to study the effects of reactivation on fault geometry, structure and geomorphology as the graben has a well-documented polyphase history of extension (Castaing, 1991; Chisenga et al., 2019) and in the current rift phase, the syn-rift sediments are thin and fault exposures are not hidden by any post-rift sediments (e.g. Hodge et al., 2019; Williams et al., 2019). We begin by describing the tectonic history of the region, before analysing the current activity, geometry, structure and geomorphology of the fault. In doing so, we assess how reactivation of pre-existing fabrics and

heterogeneities affect the evolution of a rift border fault and discuss implications for the tectonic geomorphology of reactivated basin-bounding faults.

2. Tectonic History

The Thyolo fault bounds the north-eastern edge of the Lower Shire graben, which is located at the southern end of the largely amagmatic Western branch of the East African Rift (EAR; Figure 1). Extension within the Western branch of the EAR initiated ~25 Ma (Roberts et al., 2012) and within southern Malawi, the extension rate is ~2 mm yr^{-1} (Stamps et al., 2018; Figure 1). The footwall of the Thyolo fault is composed of charnockitic gneiss and granitic granulites of the Mesoproterozoic Unango Terrane, part of the Mozambique Belt, with the fault located towards the southwestern edge of the terrane (Fullgraf et al. *in press*; Bloomfield, 1965; Johnson et al., 2005). The Unango Terrane likely formed in a continental volcanic arc setting at ~1 Ga, and experienced granulite facies metamorphism associated with ductile deformation shortly after emplacement (957 ± 27 Ma; Bingen et al., 2009). Within the footwall of the Thyolo fault, the present-day NW-SE striking metamorphic foliation and migmatitic banding was formed during granulite facies metamorphism and partial melting that occurred during a series of collisional events at a convergent continental margin in the Pan-African Orogeny (~710-555 Ma) and the associated amalgamation of Gondwana (Kröner et al., 2001; Johnson et al., 2005; Manda et al., 2019). In the region of the Thyolo fault, the edge of the Unango Terrane is in contact with the basement of the Southern Irumide Belt which underwent peak metamorphism between 1.06 and 1.05 Ga (Johnson et al., 2005; Westerhof et al., 2008; Karmakar and Schenk, 2016). The boundaries between terranes have been roughly mapped based on exposures within Malawi (Manda et al., 2019), but

153 because Karoo sediment have obscured the basement, the unit boundaries are
154 largely extrapolated from neighbouring Mozambique, where mapping was supported
155 by geochemical and airborne magnetic data (Bingen et al., 2009; Macey et al.,
156 2010).
157
158 ## 2.1 Previous phases of rifting
159 The Lower Shire graben contains Phanerozoic sedimentary and volcanic deposits
160 related to three regional phases of extension that occurred prior to the current rifting:
161 two distinct events during the Karoo-age (~330-180 Ma) breakup of Gondwana, and
162 a later phase during the Cretaceous (Castaing, 1991; Figure 2).
163
164 NW-SE Karoo-age extension in the Lower Shire Graben created space to deposit a
165 sequence of Late Ecca (Middle Permian) to Late Beaufort (Early Triassic) coal
166 shales, coarse grained grits, mudstones and sandstones (Figure 2c). These
167 sedimentary deposits are bound by NE-SW striking normal faults and NW-SE
168 striking dextral strike-slip faults including the Mwanza and possibly the Thyolo fault
169 (Figure 2c; Habgood, 1963; Habgood et al., 1973; Castaing, 1991).
170
171 NW-SE extension continued into the late Karoo period, when it was associated with
172 basaltic volcanism and contemporaneous emplacement of NE-SW striking dolerite
173 dykes. These dykes and volcanic deposits are collectively known as the Stormberg
174 Volcanics, which are widely observed in the footwalls of the Mwanza, Thyolo and
175 Mtumba faults (Figure 2d; Habgood, 1963; Habgood et al., 1973; Woolley et al.,
176 1979; Castaing, 1991).
177

178 At the end of the Karoo period (Late Jurassic – Cretaceous), the extension direction
179 rotated from NW-SE to NE-SW and reactivated NW-SE transtensional structures
180 established in the earlier phase of NW-SE extension as dip-slip normal faults (Figure
181 2e; Castaing, 1991). In the Lower Shire Graben, remnants from the NE-SW
182 extension are limited to sandstones in the hanging wall of the Panga and Chitsumba
183 faults (Figure 2e) and siliceous fault rock along the Namalambo Fault. These
184 sedimentary deposits form part of the Lupata series, a mix of coarse grained
185 sandstones, and rhyolitic and alkaline lavas found extensively in Mozambique (Dixey
186 and Campbell Smith, 1929; Habgood, 1963), and emplaced contemporaneously with
187 the Chilwa Alkaline Province, which involves intrusive rocks that crosscut the
188 Stormberg dykes (Macdonald et al., 1983; Woolley, 1987; Castaing, 1991; Eby et al.,
189 1995). Cretaceous activity on the Thyolo and/or Mwanza faults cannot be ruled out
190 as any Cretaceous sedimentary deposits will likely have been buried by current syn-
191 rift sediments.
192
193 ## 2.2 Present day rifting
194 Some previous studies in the region have interpreted the Thyolo fault as a
195 reactivated dextral strike-slip fault linking the Urema Graben (the southern active
196 continuation of the EARS in Mozambique) and the Zomba Graben (Castaing, 1991;
197 Chorowicz and Sorlien, 1992; Chorowicz, 2005). In other studies, the Thyolo fault is
198 considered inactive (Laõ-Dávila et al., 2015; Prater et al., 2016). However, remote
199 sensing observations have identified an active fault scarp along the Thyolo fault and
200 triangular facets at the southern end of the fault, which demonstrate that the Thyolo
201 fault is currently active (Hodge et al., 2019). A M_w5.6 earthquake in March 2018 had
202 a normal faulting focal mechanism with nodal planes aligned with the surface traces

of faults in the Lower Shire Graben (Figure 1). Williams et al. (2019) suggest that the Thyolo fault is currently active as a dip-slip normal fault oriented obliquely to the regional extension direction.

2.3 Summary

The Thyolo fault, that bounds the Lower Shire Graben, is hosted towards the edge of the Unango Terrane which underwent granulite facies metamorphism during continental collision and terrane accretion in Pan-African Orogeny resulting in a NW-SE oriented foliation. Since this time, the faults in the Lower Shire graben have been active during four distinct periods of horizontal extension. Two phases during the Karoo, a period of extension during the Cretaceous and the present phase of active rifting. Below, we describe in detail the dimensions and geometry of the fault scarp along the Thyolo fault, including factors that control fault segmentation and orientation, and analysis of the fault zone structure.

3. Fault Segmentation

3.1 Methods

We use a high resolution 12 m TanDEM-X digital elevation model (DEM) to identify different indicators of fault segmentation based on two distinct sets of criteria: map-view geometry and scarp height. Geometrical criteria for fault segmentation were identified by Zhang et al. (1991) as changes in fault strike, changes in fault width, fault branches, gaps and steps in map view. Broadly speaking, these areas of increased fault complexity are indicators of segment boundaries (DuRoss et al., 2016), and have been noted as a limiting factor for earthquake ruptures (Segall and Pollard, 1980), especially when gaps are greater than 3-5 km (Wesnousky, 2008). In

this study we mapped the fault trace in high resolution and noted prominent changes in fault strike and fault steps that may be indicative of fault segmentation.

Fault segmentation can also be defined from the profile of scarp height (e.g. Dawers and Anders, 1995; Willemse et al., 1996; Willemse, 1997; Walsh et al., 2003). In a plot of displacement vs. fault-parallel distance, the segment boundaries are located at local minima in displacement (Crone and Haller, 1991a; Dawers and Anders, 1995; Walsh et al., 2003). We used the scarp height measurements as a proxy for displacement (e.g. Morewood and Roberts, 2000; Hodge et al., 2018b, 2019; Wedmore et al., 2019) to identify segments based on local minima in the along-strike scarp height profile. We use adapted versions of the SPARTA tools (Hodge et al., 2019) to measure the height of the fault scarp along the Thyolo fault on the 12 m DEM. We differ from Hodge et al., 2019 by extracting 500 m long fault-perpendicular topographic profiles from the DEM every 12 m along the fault, which are then stacked at 100 m intervals before measuring the vertical difference between regression lines on the footwall and hanging wall surfaces. We estimate the uncertainty of each measurement by applying a Monte Carlo approach to sample 10,000 random subsets of points from the hanging wall and footwall of the fault as well as allowing the location of the fault to vary along the section of the topographic profiles identified as the fault scarp. The resulting measurements of vertical offset were then filtered using a 5 km wide moving median filter along the strike of the fault.

We also examined the Thyolo fault for any evidence of features associated with fault linkage. Where two un-linked fault segments interact, structures form such that the faults maintain laterally constant extensional strain (Walsh and Watterson, 1991).

253 The relay or transfer structures evolve as the faults overlap and link to form a
254 distinctive set of features, including 10-15° dipping ramps and breach structures that
255 link the segments and are often twisted and rotated (about a vertical axis) by the tips
256 of the overlapping, propagating faults prior to breaching (Fossen and Rotevatn,
257 2016). We analysed the strike of the fault by dividing the fault trace into 50 m long
258 sections and measuring the strike of each section from the trend of the surface trace,
259 assuming negligible topography. The orientation of pre-existing basement structures
260 were also analysed by digitising the 3D foliation measurements and strike of dolerite
261 (Stormberg) dykes in Habgood et al. (1973).
262
263 ### 3.2 Results
264 During a field campaigns in 2017 and 2018, we observed a recent fault scarp at the
265 base of the Thyolo fault's 1 km high footwall escarpment (Figure 1c). Hodge et al.
266 (2019) then identified a pseudo-continuous scarp along two structures totalling 85
267 km in length, the Thyolo and Muona faults, using high-resolution topography data,
268 but divided the fault into two separate faults. In the following sections, we consider
269 the Thyolo and Muona faults as a singular fault rather than two separate structures,
270 although we do differentiate between the Thyolo and Muona sections of the fault
271 (Figure 3). Triangular facets are visible within the high resolution topography along
272 the southeastern end of the Thyolo section and the northwestern end of the Muona
273 section (Figure 3). We observed no systematic deflection of river channels or any
274 other geomorphological features that might indicate strike-slip faulting, and we
275 therefore consider the Thyolo fault to be currently accommodating pure normal dip-
276 slip displacement (see also Williams et al., 2019). We used further field observations

277 from 2018 to ground truth the geometrical and scarp height observations from high
278 resolution topography and geological maps detailed in the following sections.
279
280 3.2.1 Map View Geometry
281 The Thyolo fault is ~85 km long and has a mean strike of 139 ± 15° (1 standard
282 deviation) dipping to the south west (Figure 3 & 4). A fault scarp was visible in the
283 high-resolution topography along the length of the fault, with gaps observed where
284 major rivers cross the fault and have eroded the scarp (Figure 3b). High-resolution
285 mapping of the scarp found seven sections along the fault which trend approximately
286 perpendicular to the main fault (Figure 4c). These NE-SW oriented sections have a
287 mean strike of 034 ± 8° (black lines in Figure 4) with five sections dipping to the
288 northwest and two sections dipping to the southeast. The dip angle of these NE-SW
289 oriented sections is unknown but is likely steep based on the slope of the facet in the
290 escarpment above (Figure 5). The most prominent of these NE-SW sections forms a
291 4.8 km near orthogonal link between the Thyolo and Muona sections (Figure 5). The
292 ~69 km long Thyolo and the ~28 km long Muona sections overlap by ~10 km and are
293 separated by this 4.8 km long strike-perpendicular section, which we refer to as the
294 Chisumbi section. The six other scarp sections that strike perpendicular to the main
295 fault are each <500 m long.
296
297 The mean strike of the foliation within the footwall of the Thyolo fault is 140 ± 37°
298 with a dip of 56 ± 12° to the SW (Figure 4 & 5). This is sub parallel to the mean strike
299 of the fault scarp (139 ± 15°) and the dip of the fault (assuming Andersonian
300 mechanics). Conversely, the mean strike of the dolerite dykes in the fault's footwall is
301 037 ± 9° which is the same (within error) as the strike-perpendicular sections of the

fault (034 ± 8°; including the Chisumbi section). Our field measurements at four localities along the Thyolo Fault indicate that the dykes are vertically dipping (Figure 3a). Thus, the main sections of the Thyolo fault are sub-parallel to the metamorphic foliation and dip in the same direction. In addition, the foliation dips at an angle that is within the typical range of active normal fault dips (45°-60°; Collettini and Sibson, 2001; Figure 4). However, in places the fault trace crosscuts the foliation at a high angle and is instead subparallel to the surface trace of footwall dolerite dykes (Figure 5).

3.2.2 Scarp Height

The median height of the fault scarp along the Thyolo fault is 18.6 ± 7.7 m (calculated as the median of the 5 km moving median plotted in Figure 4). The along strike profile of the scarp height measurements shows two scarp height minima (besides the tips of the fault; Figure 4b). The distance from fault tip to the first minimum is 28 km with a median scarp height of 24.9 ± 9.0 m in this portion of fault (Figure 4b). The next portion of fault is 15 km long and has a median scarp height of 20.8 ± 6.3 m. The final portion is 48 km long with median scarp height of 17.8 ± 6.5 m (Figure 4b). None of the scarp height minima identified from the scarp height profile coincide with fault geometrical changes, i.e. the short segments that strike perpendicular to the main fault (Figure 4).

3.2.3 The Chisumbi Section

The 4.8 km Chisumbi sections links the Muona and Thyolo sections and is oriented at 105 ± 17° to the strike of the main fault but subparallel to the dolerite dykes (Figure 5). Along this linking section, we observed a 19.0 ± 4.2 m high scarp (profile

D in Figure 3b; Figure 4). This height (yellow triangle in Figure 4b) is within the error bounds of the scarps found along the adjacent Muona and Thyolo sections. Thus, the fault scarp along Chisumbi section has a similar height to the bounding sections that it is approximately perpendicular to.

One possibility is that the Chisumbi section is a breached relay ramp. However, the morphology of the Chisumbi section is subtly different from the typical form of relay ramps. To show this we compare structural features from the footwall of the Chisumbi section with both the bounding Muona and Thyolo sections and to the expected geometry of relay ramps from global examples. The dolerite dykes within the overlapping zone have a strike of 031 ± 9° whereas the strike of the dolerite dykes outside the overlap zone is 038 ± 9° (Figure 5b). Thus, as these values are within the error bounds of each other, the average trace of dykes within the overlapping zones have either no rotation or a slight anticlockwise rotation around a vertical axis (Figure 5b). A clockwise rotation would be expected for the overlapping geometry (Figure 9a), and therefore, the observations indicate little strain has been induced during the process of fault linkage. Furthermore, breaching of a relay ramp normally occurs when a 10-15° ramp has formed (Figure 9b), with distinctive morphologies depending on the location of the breach (Figure 9a; Fossen and Rotevatn, 2016). The dip of the topography (excluding the facet slope above the fault scarp) in this overlapping zone is 2° (Figure 5c), so the Chisumbi scarp is unlikely to a breached relay ramp.

The Chisumbi section has a unique geomorphological signature, unlike that seen in typical ramp geometries (Densmore et al., 2003). While river channels often bend

352 around propagating fault tips to avoid impinging zones of high rock uplift rates, the
353 river channels of the Thyolo run perpendicular to the fault trace and show few signs
354 of bending in the footwall of the fault. An important exception to this is the Chizimbi
355 River which flows to the northwest along the from the southern end of the Thyolo
356 fault, and marks the northern extent of the Chisumbi section (Figure 9). Such a
357 regional drainage network is not predicted by the lithospheric deformation associated
358 with relay ramp formation or longer-term evolution (Densmore et al., 2003 and Figure
359 9a), and thus requires a different formation mechanisms. A further consequence of
360 this unusual pattern of drainage is that alluvial fans located in the hanging wall of the
361 inboard Thyolo section extend much further from the fault trace (~5km) than alluvial
362 fans on the outboard Muona section (~2 km; see contours in Figure 5b). We discuss
363 the origins of this structure further in section 5.1.
364
365 ## 4. Damage zone and fault core structure of the Thyolo fault
366 ### 4.1 Sample collection and analysis
367 The footwall damage zone of the Thyolo fault zone is exposed at four localities:
368 Kalulu, Kanjedza, Mbewe, and Muona (Figure 3). At each exposure, we made
369 lithological and structural observations along transects from the fault scarp to
370 distances up to 280 m from the fault. In addition, samples were collected at Kalulu (n
371 = 5) and Kanjedza (n = 11) respectively for microstructural and compositional
372 analyses. To locate the samples relative to a line perpendicular to the fault's
373 orientation (139/60 SW), as well as to survey the fault scarp and footwall structures,
374 we captured aerial photography using a DJI Phantom 3 drone with onboard GPS
375 positioning. At Kalulu, images were captured in a regular grid with three different
376 flight plans taking photos from a range of viewing angles and elevations using the

software DJI Groundstation Pro. At Kanjedza and Mbewe, drone photography was augmented with images from a handheld Canon Powershot SX280 HS camera with inbuilt GPS. Digital elevation models and orthophotos were constructed from these images using the structure-from-motion technique within Agisoft Metashape Pro (Johnson et al., 2014). The three samples furthest from the fault at Kanjedza were outside the drone survey and on the escarpment itself. The locations of these samples were instead measured with a handheld GPS, and their distance from the Thyolo fault was measured based on the distance between the sample and the fault projected from its surface trace at a dip of 60° (see figure S1 in the supplementary material).

Thin sections were made of all samples for microstructural analysis and fracture density measurements. At both sites, the fault is roughly foliation parallel, and so by cutting samples along the foliation dip-direction, they can be approximated as being perpendicular to the fault plane. Some samples did not contain a discernible foliation; for these samples, thin sections were instead cut at random orientations. Note that differences in thin section orientation do not appear to influence our microfracture density measurements (Figure 8h).

To measure microfracture density (defined as fracture length per sample area in mm^{-1}), three 10-15 mm^2 sample areas were selected in each thin section. These were derived by photographing the area at 5x magnification in plane polarised light (PPL) and cross polarised light (XPL) under a petrographic microscope, and then stitching the photomicrographs together using the MosaicJ plugin in ImageJ. To

minimise the influence of orientation bias in fracture density quantification (e.g. Terzaghi, 1965), each sample area had a square shape.

Fractures were traced based on interpretations of both the PPL and XPL images of the sample area at a constant 200% zoom. Only fractures within quartz or feldspar grains were traced, to allow comparison between lithologically diverse samples, and fractures whose centres were not in the sample area were removed to reduce censoring effects (Zeeb et al., 2013). Cleavage sets could be differentiated from fractures in feldspar grains as cleavages tended to be deflected by twinning or form intragranular systematic sets at 90° to each other (Figure 8b). The total length of fracture traces in each sample area was calculated using FracPaQ 2.2 (Healy et al., 2017). To determine fracture density, total fracture length was then divided by sample area, which was calculated after filtering regions in the image that constituted non-quartzofeldspathic grains, or missing areas of the thin section that had been lost during sample preparation. The fracture density for each thin section was then calculated from the area-weighted average of its three sample areas.

4.2 Observations

The contact between footwall gneisses and hanging-wall sediments is exposed at Kalulu (Figure 6). These two units are separated by a 0.7 m thick incohesive unit of white to minty green massive fault gouge. In thin exposure, the gouge contains a brown clay-rich matrix with subangular to subrounded clasts of intensely fractured quartz up to 3 mm in size (Figure 6b). The relative proportions of matrix and clast by area are estimated to be 90% and 10% respectively (see Figure S2) This unit

425 constitutes the fault core (sensu Caine et al., 1996), which was only found exposed
426 at this location.
427
428 At Kalulu, the fault core is surrounded by a 5-15 m thick incohesive unit of
429 quartzofeldspathic granulite and hornblende gneiss. At the other three other localities
430 a 15-45 m wide unit of incohesive biotite ± hornblende ± pyroxene gneiss is found in
431 the exposure closest to the scarp (Figure S3). Metamorphic foliation and pegmatite
432 veins are still preserved within the incohesive gneisses; however, they may be
433 locally separated by < 0.6 m along minor faults (Figure 6).
434
435 In the incohesive gneisses at Kanjedza, a 2 m wide ductile reverse shear zone has
436 been exploited by a NW-SE striking dyke of unknown age (Figure 7). A minor fault
437 with a normal sense of slip has then subsequently offset this dyke. At Mbewe, a 50
438 cm thick steeply dipping foliated fault gouge is present 10 m into the footwall and is
439 parallel to the scarp. This gouge represents a fault that juxtaposes charnockite and
440 hornblende gneisses (Figure S3). The hornblende gneiss foliation here is locally
441 folded. At distances of more than 50-280 m from the fault at Kanjedza, Kalulu, and
442 Muona, intact biotite ± hornblende gneisses are crosscut by vertical NE-SW striking
443 dolerite dykes.
444
445 In thin sections made from the incohesive gneisses (i.e. within 45 m of the fault) at
446 Kanjedza and Kalulu, quartz and feldspar grains exhibit fracture densities of 2.3-4.8
447 mm^{-1} (Figure 8). These fractures are oblique to the foliation, which is defined at the
448 microscale by alternating quartzofeldspathic and biotite ± hornblende ± garnet
449 bands, in which elongate biotite grains are aligned to and also define a foliation

subparallel to the compositional banding. Fractures are generally intragranular and closed, with some rare cases of them hosting biotite or calcite mineralisation (Figure 8d). Open fractures are also observed and most prevalent in samples closest to the fault (Figure 8d). Microscale fracture density 50-280 m from the fault within the intact gneisses is 0.9-2.2 mm^{-1}, and fractures are parallel to the foliation (Figure 8f). We interpret the 15-45 m wide unit of incohesive gneiss with a relatively high fracture density, foliation-oblique fractures, and that has only accommodated a minor amount of displacement, as the footwall damage zone (sensu Caine et al., 1996) of the Thyolo fault.

No systematic decay in fracture density with distance from the fault is observed within the damage zone (Figure 8), which may reflect that samples are not consistently oriented with respect to the fault, and/or variations in grain size and composition. Alternatively, it may be due to the influence of minor faults within the damage zone; the highest fracture density is recorded ~42 m from the fault at Kanjedza, where a dyke has been offset by a minor fault, and abundant biotite veins are observed (Figure 8d). It is unclear whether this relatively high fracture density can be attributed to dyke emplacement or displacement on the minor fault The microfracture density increase inside the damage zone relative to the background level is relatively minor (Figure 8h*;* compare with (Wilson et al., 2003; Mitchell and Faulkner, 2009). However, it is difficult to assess if this is representative of a relatively low fracture density in the damage zone, or if it may reflect selective sampling of more cohesive, intact portions of the damage zone for thin section preparation and fracture density quantification.

5. Discussion

Topographic features including an 18.6 ± 7.7 m fault scarp and triangular facets indicate that the Thyolo fault has been reactivated during the current stage of East African Rifting. Whereas the Thyolo fault is dominantly subparallel to the metamorphic foliation, there are notable sections where the strike turns by 90˚ and therefore trends subparallel to Stormberg-age dolerite dykes (Figure 5). Here we discuss what defines fault segmentation where two different indicators of segmentation (geometrical changes and displacement profile minima) yield different numbers and locations of segment boundaries. We also discuss the fault zone structure in comparison to other rift-related faults, and how the reactivation of shallow crustal heterogeneities and deeper viscous deformation may combine to affect surface trace geometry. To conclude, we propose a model for the combined effects of pre-existing structures and dynamic stresses on fault reactivation.

5.1 Fault segmentation

Scarp height minima and changes in surface fault geometry are generally considered indicators of fault segment boundaries (Crone and Haller, 1991b; Machette et al., 1991; Peacock and Sanderson, 1991; Crider and Pollard, 1998; Mortimer et al., 2007, 2016; Fossen and Rotevatn, 2016). These factors identified matching segment numbers and boundary locations along the Bilila-Mtakataka fault in southern Malawi (Hodge et al., 2018b; see Figure 1 for location). However, along the Thyolo fault, the locations of scarp height minima do not coincide with changes in surface fault geometry (Figure 4). The sections that trend perpendicular to the overall strike range in length from 170 m to 4.8 km, but only one of the sections (the Chisumbi section) is likely long enough to be considered a geometrical segment boundary (i.e. ≥ ~3-5 km;

Wesnousky, 2008). This geometry has been used to argue that the Thyolo and Muona sections are different faults (Hodge et al., 2019). However, a fault scarp along the Chisumbi section links the Thyolo and Muona sections, and the height of this scarp is in the same range as scarps along the bounding Thyolo and Muona sections (Figure 3b, profile D; Figure 4b). This implies that during the recent events that formed the scarp, slip likely propagated along and through the 4.8 km long, ~100° bend in the fault. Given the ~600 m high escarpment and triangular facets along the Chisumbi section it is also likely that slip has propagated along and through this section over longer geological time (Figure 9c). This suggests that on faults that have reactivated pre-existing fabrics, purely geometrical criteria may not adequately identify fault segmentation for seismic hazard purposes. This is in contrast to the Wasatch fault zone, USA, where DuRoss et al. (2016) suggest that displacement profiles have limited value for identifying segment boundaries that restrict earthquake ruptures.

The Chisumbi section lacks evidence for distributed strain in the area between the tips of the Thyolo and Muona sections it links (Figure 9). There is no or minor anticlockwise rotation of dykes in the footwall of the Chisumbi section and the slope dips at a very shallow angle (~2°). This suggests that little strain accumulated within this section prior to the bounding Thyolo and Muona sections becoming linked (Willemse et al., 1996; Peacock and Sanderson, 1991; Densmore et al., 2003; Fossen and Rotevatn, 2016; Figure 9). Through this lack of evidence for the development of a relay ramp, we therefore propose that the Thyolo and Muona sections are linked by weak structures that have been activated in the shallow upper crust, but which do not operate as permanent barriers to earthquake rupture and

propagation (Figure 9d). The Chisumbi linkage zone also differs in geomorphology from a typical relay ramp (e.g. Gawthorpe and Leeder, 2000; Densmore et al., 2003), with no axial ramp drainage, but also no transverse ramp drainage (Figures 5 and 9). Instead the main drainage channel runs along the overlapping tip of the Thyolo section leading to an abnormal configuration to the hanging wall alluvial fans (Figures 5 and 9). This suggests that where pre-existing structures affect the reactivation of extensional basins, unusual patterns of sediment transport and deposition may be observed.

5.2 Thyolo fault zone structure

Normal faults grow incrementally by a combination of accumulation of displacement, linkage of segments, and increase in length, such that fault growth, structure, and geometry are closely linked (e.g. Cartwright et al., 1996; Childs et al., 2017; Hodge et al., 2018a; Rotevatn et al., 2019). Along the Thyolo fault, we cannot place definitive constraints on the total damage zone width or displacement, because we lack hanging wall exposures and distinct marker horizons. Nevertheless, given its ~1 km (Figure 1c) escarpment height and a fault dip of ~ 60° (Williams et al., 2019), it must have accommodated >1.2 km of net dip-slip displacement. Furthermore, although damage zones are typically asymmetric, the hanging wall damage zone rarely exceeds three times the width of the footwall damage zone where both are exposed (Beach et al., 1999; Shipton and Cowie, 2001; Berg and Skar, 2005; Kristensen et al., 2016), and in some cases, the damage zone may be wider in the footwall than the hanging wall (Biegel and Sammis, 2004). With a footwall damage zone 15-45 m wide, we therefore suggest that the entire width of the Thyolo fault damage zone is between 15 and 180 m.

Given a displacement of 1.2 km, the Thyolo fault damage zone width is within the range of displacement vs damage zone width determined from compilations of all fault types (Torabi and Berg, 2011; Savage and Brodsky, 2011). However, there is considerable scatter in these plots owing to variations in the fault kinematics, lithology, and the depth of faulting. A more instructive comparison may therefore be to the Djomberg fault in Greenland, which offers a rare example of a well exposed rift border fault (3 km throw) in crystalline metamorphic basement rocks (Kristensen et al., 2016). The Djomberg fault's damage zone extends 600 m into the footwall (Kristensen et al., 2016), which is 10 times further than the Thyolo fault, although both faults are parallel to a gneissic footwall foliation.

Fault core thickness also scales with displacement, with the km-scale slip along the Thyolo fault predicted to result in a fault core 1-10 m thick (Torabi and Berg, 2011; Torabi et al., 2019). Across the Djomberg fault slip is accommodated across several <50 cm thick strands of gouge and breccia in a 200 m wide zone within the fault's footwall (Kristensen et al., 2016). However, along the Thyolo fault, the fault core is 0.7 m thick at Kalulu (Figure 6), and although the fault core is not exposed elsewhere, the footwall damage zone extends to within 15 m of the scarp at Kanjedza placing a maximum constraint on footwall fault core thickness at 15 m here. At Mbewe (see Figure 3 for location), the damage zone extends to within 1 m of the scarp; however, there is a secondary fault strand 10 m into the footwall. In summary, the damage zone width of the Thyolo fault is therefore comparable to other faults with km scale displacement; however, it is relatively narrow compared to

another example of a rift border fault, and its slip is localised into an anomalously narrow fault core given the displacement it has accommodated.

5.3 Mechanism of fault reactivation

Within amagmatic portions of the East African Rift System, immature faults (Biggs et al., 2010), strong, cold intact crust (Fagereng, 2013) and low b-values recorded during seismic sequences (Gaherty et al., 2019; Lavayssière et al., 2019) are all suggestive of high differential stress in the region. Furthermore, gouge sampled from the fault core at Kalulu does not contain significant amounts of frictionally weak minerals (Williams et al., 2019), and deformation experiments on representative lithologies from the Malawi Rift indicate that they are frictionally strong (coefficient of friction, μ_s >0.55; Hellebrekers et al., 2019). However, the fault is generally oriented parallel or sub-parallel to basement foliation and possibly also Karoo-age dykes (Figure 4-5). These structures may provide low cohesion planes for frictional reactivation, even if they are slightly oblique to the minimum principal compressive stress (Williams et al., 2019).

Previous studies indicate that complex surface patterns of normal faults may connect to a more planar feature at depth (e.g. Graymer et al., 2007; Walker et al., 2017; Hodge et al., 2018). We suggest that interlinked mechanisms of reactivation and dynamic stress reorientation along the Thyolo fault may explain the geometry of fault sections orientated perpendicular to the strike of the main fault and sub-parallel to Stormberg dykes. Firstly, the overlapping geometry between the Thyolo and Muona sections may have been established early in the growth history of the Thyolo fault. This overlapping geometry favours high angle link structures formed due to

599 coseismic Coulomb stress changes on the bounding faults (Hodge et al., 2018a).,
600 rather than obliquely oriented breached relay ramps or the creation of a fault bend.
601 These links may have originated as transform faults, and later seen reactivation as
602 normal faults, although no evidence for transform motion is preserved. Secondly, slip
603 on orthogonal structures may have been favoured by the presence of dolerite dykes
604 perpendicular to the Thyolo fault (Figure 5a), although linking segments coinciding
605 with a pre-existing dyke have not been directly observed. Dolerite dykes emplaced
606 within Karoo sediments in South Africa have been reported to induce increased
607 brittle damage reducing cohesion along the dyke-basement contact zone (Senger et
608 al., 2015). It is therefore possible that co-seismic stress changes on overlapping
609 faults favoured shallow activation of low-cohesion zones at the edge of the pre-
610 existing dykes.
611
612 We suggest that low cohesion planes may play an important role in controlling fault
613 geometry in the shallow crust. Though significant fluid flow can result in fault zone
614 cohesion regaining its strength relatively quickly (10^3-10^5 years; Tenthorey and Cox
615 2006), this recovery mechanism is unlikely along the Thyolo fault as the crust in
616 Malawi has been dehydrated during one or more previous episodes of high grade
617 metamorphism (Fagereng, 2013). Furthermore, we do not see fault zone fluid flow
618 indicators in our microstructural and field observations (e.g. no extensive vein
619 networks or fault zone alteration; Wästeby et al., 2014; Williams et al., 2017) and
620 instead find evidence for an incohesive ‘unhealed’ fault damage zone (Figures 7 &
621 8).
622

While the fault may follow near-surface weaknesses, this mechanism is less applicable at depths where cohesion is maintained or confining stresses too high for frictional failure. The Thyolo fault is located at or towards the edge of the Unango Terrane, although the exact nature and location of this boundary is uncertain. If it is similar to other high metamorphic grade boundaries, it could represent an existing shear zone that is viscously weak because of small grain size (Watterson, 1975; Fliervoet et al., 1997; Stenvall et al., 2019), foliation of interconnected low viscosity minerals (Handy, 1990; Montési, 2013), crystal-preferred orientations conducive to plastic flow (Poirier, 1980), or provide a competency contrast across the boundary that leads to increased stress and therefore a localisation of strain (Goodwin and Tikoff, 2002). Thus, we suggest that heterogeneity in viscous processes associated with ductile structures can localise strain beneath the brittle crust along the Thyolo fault. Consequently, we consider that the Thyolo fault follows a deep-seated ductile weakness associated with the boundary of the Unango Terrane at mid-crustal level and exploits low cohesion, well oriented foliation planes linked by dyke edges at the near surface (Figure 10).

A deep-seated ductile control on the overall fault structure and displacement may explain why along the Thyolo fault, shallow structures have induced changes in fault geometry that are not reflected in the scarp height. Hence, although many faults, including the Bilila-Mtakataka fault in the Makanjira Graben (Figure 1; Hodge et al., 2018b), show both displacement minima and geometrical changes (or structural complexity) at the same locations (Peacock and Sanderson, 1991; Dawers and Anders, 1995; Walsh et al., 2003), where a fault experiences depth-dependent control on its structures, these two segmentation criteria are unlikely to agree. This

presents a challenge when segmentation criteria based on shallow structures is used for assessing earthquake magnitudes for seismic hazard analyses (e.g. Field et al., 2009; Petersen et al., 2015; Valentini et al., 2019): where depth-dependent segmentation is not correctly identified, multi-segment and multi-fault ruptures such as those observed in the 2016 earthquakes in central Italy (M_w6.2, 6.1 & 6.6) and Kaikoura, New Zealand (M_w7.8) or the 2010 M_w7.2 El Mayor-Cucapah, Mexico earthquake (Wei et al., 2011; Hamling et al., 2017; Walters et al., 2018) may become more likely than is apparent from superficial indicators of fault segmentation.

A depth-dependent combination of structural controls can also explain other observations along the Thyolo fault, including its slightly oblique orientation to the regional extension direction yet apparent dip-slip kinematics (Philippon et al., 2015; Hodge et al., 2018b; Williams et al., 2019) and its continual reactivation under a diverse range of previous extensional directions within the Lower Shire Graben (Castaing, 1991). Furthermore, localised slip and a narrow damage zone is also observed for other faults that follow a pre-existing foliation (Heermance et al., 2003; Zangerl et al., 2006). Thus, through collective evidence for structural controls and fast fault growth in a localised fault core, we prefer an interpretation where fault geometry is controlled by heterogeneities in the viscous lower crust, with the brittle upper crust having a secondary control affecting the surface trace. We recognise the model where the primary control on rift growth is lithospheric strength (Ebinger et al., 1991); however, while the total fault length may indeed reflect a thick elastic crust, the detailed fault geometry appears affected by documented structural elements.

5.4 Comparison with other continental rifts and grabens

That shallow brittle structures only have a superficial, geometric effect on fault segmentation is important, because geometrical criteria have been used to define fault segments for seismic hazard purposes (Crone and Haller, 1991a; Lettis et al., 2002; Wesnousky, 2008). If local fabrics only control the shallow orientation of the fault, this also explains why faults in Malawi have been simultaneously observed to crosscut and follow the metamorphic foliation (Hodge et al., 2018b). Furthermore, it explains the difference between the Lower Shire Graben, where the largest topographic relief indicates that the majority of displacement occurs on the border fault (the Thyolo fault; Fig. 1), and the Zomba Graben to the north, where displacement is distributed more evenly between border and intrabasin faults (Wedmore et al., 2019). Lateral heterogeneity within the lower crust beneath the Zomba Graben has been inferred to cause this more heterogeneous strain distribution, possibly by multiple localised shear zones at depth guiding distributed deformation in the upper crust and at the surface (Wedmore et al., 2019). This is a preferred explanation for strain distribution in the Zomba Graben, as it is located *within* the Unango Terrane. In contrast, the Lower Shire Graben is located towards the edge of the terrane boundary and hence the deformation may localise towards the terrane edge. This localised deformation and fast growth and linkage of a border fault is comparable to the Okavango rift, which is also inferred to be localised along a long-lived pre-existing crustal-scale weak zone (Kinabo et al., 2007, 2008).

The northern North Sea basin is another example of a multiphase rift where faults are hosted in crystalline basement rocks. Here, lithospheric thinning and heating, as well as stress feedbacks between growing faults, control the rift-scale localisation of strain, with pre-existing shallow brittle faults thought to have little control on

698 reactivation (Cowie et al., 2005; Claringbould et al., 2017). Our results are consistent
699 with the inference that pre-existing shallow structures and fabrics have only minor
700 control on reactivation, and that pre-existing upper crustal faults play only a minor,
701 superficial role in controlling subsequent rift geometries in crystalline, dry, continental
702 crust. This differs from studies where a major role in rift evolution has been
703 suggested for upper crustal faults (e.g. Bellahsen & Daniel, 2005; Duffy et al., 2015;
704 Heilman et al., 2019; Katumwehe et al., 2015; Laõ-Dávila et al., 2015; Whipp et al.,
705 2014). This confirms the need to consider the scale and depth dependence of the
706 influence of pre-existing structures when assessing fault reactivation, where the pre-
707 existing weaknesses may control macro- but not meso-scale structural development
708 (Kirkpatrick et al., 2013; Samsu et al., 2020).
709
710 ## 6. Conclusion
711 The Thyolo fault is the major border fault within the Lower Shire Graben, which has
712 experienced Neoproterozoic continental collision and at least three previous periods
713 of Phanerozoic rifting. Using high resolution topography, we mapped the surface
714 trace of the Thyolo fault to study the reactivation of the fault within the current period
715 of rifting in East Africa. Long sections of the fault have a NW-SE strike, but these are
716 separated by short sections that strike NE-SW. The largest NE-SW section is 4.8 km
717 long, which is normally considered long enough to define a separate fault segment
718 that accumulates displacement differently from adjacent segments. However, based
719 on along strike variations of the height of the active fault scarp, we find three main
720 segments, each with a scarp approximately 20 m high. The segment boundaries
721 defined by the scarp height do not correspond to prominent geometrical changes in
722 fault strike that are normally considered indicative of segment boundaries. We find

723 that the fault and pre-existing foliation are broadly parallel, whereas the strike of the
724 short sections orientated NE-SW matches the strike of dykes emplaced during a
725 previous period of rifting in the Karoo. Using field and microstructural observations of
726 the Thyolo fault's footwall, we estimate that the entire fault zone is between 15-180
727 m wide, comparable to other faults of similar displacement, but considerably
728 narrower than another example of a rift bounding fault in crystalline metamorphic
729 basement (the Djomberg fault, Greenland). All these observations suggest that the
730 shallow portion of the fault is reactivating well-oriented foliation planes and
731 perpendicularly oriented dyke contacts that act as low-cohesion surfaces in the
732 shallow crust. However, these pre-existing structures are not reflected in the
733 displacement-length profile, and are therefore interpreted as not being able to affect
734 the growth and segmentation of the reactivated fault. Instead, we suggest that the
735 fundamental control on the growth and displacement accumulation of this rift border
736 fault is controlled by reactivation in the viscous regime, of mid-crustal ductile
737 heterogeneities associated with the edge of the Unango Terrane.
738
739 ## 7. Acknowledgements
740 This work was funded by the EPSRC project 'Prepare' (EP/P028233/1), funded
741 under the Global Challenges Research Fund. We thank Kondwani Dombola for his
742 assistance with fieldwork planning and logistics. TanDEM-X data were obtained via
743 DLR proposal DEM_GEOL0686.
744

References

Beach, A., Welbon, A.I., Brockbank, P.J., and McCallum, J.E., 1999, Reservoir damage around faults: Outcrop examples from the Suez rift: Petroleum Geoscience, v. 5, p. 109–116, doi:10.1144/petgeo.5.2.109.

Bellahsen, N., and Daniel, J.M., 2005, Fault reactivation control on normal fault growth: An experimental study: Journal of Structural Geology, v. 27, p. 769–780, doi:10.1016/j.jsg.2004.12.003.

Berg, S.S., and Skar, T., 2005, Controls on damage zone asymmetry of a normal fault zone: Outcrop analyses of a segment of the Moab fault, SE Utah: Journal of Structural Geology, v. 27, p. 1803–1822, doi:10.1016/j.jsg.2005.04.012.

Biegel, R.L., and Sammis, C.G., 2004, Relating Fault Mechanics to Fault Zone Structure, *in* Advances in Geophysics, p. 65–111, doi:10.1016/S0065-2687(04)47002-2.

Biggs, J., Nissen, E., Craig, T., Jackson, J., and Robinson, D.P., 2010, Breaking up the hanging wall of a rift-border fault: The 2009 Karonga earthquakes, Malawi: Geophysical Research Letters, v. 37, p. 1–5, doi:10.1029/2010GL043179.

Bingen, B., Jacobs, J., Viola, G., Henderson, I.H.C., Skår, Ø., Boyd, R., Thomas, R.J., Solli, A., Key, R.M., and Daudi, E.X.F., 2009, Geochronology of the Precambrian crust in the Mozambique belt in NE Mozambique, and implications for Gondwana assembly: Precambrian Research, v. 170, p. 231–255, doi:10.1016/j.precamres.2009.01.005.

Bloomfield, K., 1965, The geology of the Zomba Area: Bulletin of the Geological Survey, Malawi, v. 16.

Buck, W.R., 1991, Modes of continental lithospheric extension: Journal of Geophysical Research: Solid Earth, v. 96, p. 20161–20178,

770 doi:10.1029/91JB01485.
771 Caine, J.S., Evans, J.P., and Forster, C.B., 1996, Fault zone architecture and
772 permeability structure: Geology, v. 24, p. 1025–1028, doi:10.1130/0091-
773 7613(1996)024<1025:FZAAPS>2.3.CO;2.
774 Cartwright, J.A., Mansfield, C., and Trudgill, B., 1996, The growth of normal faults by
775 segment linkage: Geological Society, London, Special Publications, v. 99, p.
776 163–177, doi:10.1144/GSL.SP.1996.099.01.13.
777 Castaing, C., 1991, Post-Pan-African tectonic evolution of South Malawi in relation to
778 the Karroo and recent East African rift systems: Tectonophysics, v. 191, p. 55–
779 73, doi:10.1016/0040-1951(91)90232-H.
780 Childs, C., Holdsworth, R.E., Jackson, C.A.L., Manzocchi, T., Walsh, J.J., and
781 Yielding, G., 2017, Introduction to the geometry and growth of normal faults:
782 Geological Society Special Publication, v. 439, p. 1–9, doi:10.1144/SP439.24.
783 Childs, C., Manzocchi, T., Walsh, J.J., Bonson, C.G., Nicol, A., and Schöpfer, M.P.J.,
784 2009, A geometric model of fault zone and fault rock thickness variations:
785 Journal of Structural Geology, v. 31, p. 117–127, doi:10.1016/j.jsg.2008.08.009.
786 Chisenga, C., Dulanya, Z., and Jianguo, Y., 2019, The structural re-interpretation of
787 the Lower Shire Basin in the Southern Malawi rift using gravity data: Journal of
788 African Earth Sciences, v. 149, p. 280–290,
789 doi:10.1016/j.jafrearsci.2018.08.013.
790 Chorowicz, J., 2005, The East African rift system: Journal of African Earth Sciences,
791 v. 43, p. 379–410, doi:10.1016/j.jafrearsci.2005.07.019.
792 Chorowicz, J., and Sorlien, C., 1992, Oblique extensional tectonics in the Malawi
793 Rift, Africa: Geological Society of America Bulletin, v. 104, p. 1015–1023,
794 doi:10.1130/0016-7606(1992)104<1015:OETITM>2.3.CO;2.

795 Claringbould, J.S., Bell, R.E., Jackson, C.A.L., Gawthorpe, R.L., and Odinsen, T.,
796 2017, Pre-existing normal faults have limited control on the rift geometry of the
797 northern North Sea: Earth and Planetary Science Letters, v. 475, p. 190–206,
798 doi:10.1016/j.epsl.2017.07.014.
799 Collettini, C., and Sibson, R.H., 2001, Normal faults, normal friction? Geology, v. 29,
800 p. 927, doi:10.1130/0091-7613(2001)029<0927:NFNF>2.0.CO;2.
801 Cowie, P.A., 1998, A healing-reloading feedback control on the growth rate of
802 seismogenic faults: Journal of Structural Geology, v. 20, p. 1075–1087,
803 doi:10.1016/S0191-8141(98)00034-0.
804 Cowie, P.A., and Scholz, C.H., 1992a, Displacement-length scaling relationship for
805 faults: data synthesis and discussion: Journal of Structural Geology, v. 14, p.
806 1149–1156, doi:10.1016/0191-8141(92)90066-6.
807 Cowie, P.A., and Scholz, C.H., 1992b, Growth of faults by accumulation of seismic
808 slip: Journal of Geophysical Research, v. 97, p. 11085, doi:10.1029/92JB00586.
809 Cowie, P.A., and Scholz, C.H., 1992c, Physical explanation for the displacement-
810 length relationship of faults using a post-yield fracture mechanics model: Journal
811 of Structural Geology, v. 14, p. 1133–1148, doi:10.1016/0191-8141(92)90065-5.
812 Cowie, P.A., Underhill, J.R., Behn, M.D., Lin, J., and Gill, C.E., 2005, Spatio-
813 temporal evolution of strain accumulation derived from multi-scale observations
814 of Late Jurassic rifting in the northern North Sea: A critical test of models for
815 lithospheric extension: Earth and Planetary Science Letters, v. 234, p. 401–419,
816 doi:10.1016/j.epsl.2005.01.039.
817 Craig, T.J., Jackson, J.A., Priestley, K., and Mckenzie, D., 2011, Earthquake
818 distribution patterns in Africa: Their relationship to variations in lithospheric and
819 geological structure, and their rheological implications: Geophysical Journal

International, v. 185, p. 403–434, doi:10.1111/j.1365-246X.2011.04950.x.

Crider, J.G., and Pollard, D.D., 1998, Fault linkage: Three-dimensional mechanical interaction between echelon normal faults: Journal of Geophysical Research: Solid Earth, v. 103, p. 24373–24391, doi:10.1029/98jb01353.

Crone, A.J., and Haller, K.M., 1991a, Segmentation and the coseismic behavior of Basin and Range normal faults: examples from east-central Idaho and southwestern Montana, U.S.A.: Journal of Structural Geology, v. 13, p. 151–164, doi:10.1016/0191-8141(91)90063-O.

Crone, A.J., and Haller, K.M., 1991b, Segmentation and the coseismic behavior of Basin and Range normal faults: examples from east-central Idaho and southwestern Montana, U.S.A.: Journal of Structural Geology, v. 13, p. 151–164, doi:10.1016/0191-8141(91)90063-O.

Daly, M.C., Chorowicz, J., and Fairhead, J.D., 1989, Rift basin evolution in Africa: The influence of reactivated steep basement shear zones: Geological Society Special Publication, v. 44, p. 309–334, doi:10.1144/GSL.SP.1989.044.01.17.

Dawers, N.H., and Anders, M.H., 1995, Displacement-length scaling and fault linkage: Journal of Structural Geology, v. 17, p. 607–614, doi:10.1016/0191-8141(94)00091-D.

Dawers, N.H., Anders, M.H., and Scholz, C.H., 1993, Growth of normal faults: displacement-length scaling: Geology, v. 21, p. 1107–1110, doi:10.1130/0091-7613(1993)021<1107:GONFDL>2.3.CO;2.

Densmore, A.L., Dawers, N.H., Gupta, S., Allen, P.A., and Gilpin, R., 2003, Landscape evolution at extensional relay zones: Journal of Geophysical Research: Solid Earth, v. 108, p. 1–15, doi:10.1029/2001jb001741.

Dixey, F., and Campbell Smith, W., 1929, The rocks of the Lupata Gorge and the

845 north side of the lower Zambezi: Geological Magazine, v. 66, p. 241–259.
846 Duffy, O.B., Bell, R.E., Jackson, C.A.L., Gawthorpe, R.L., and Whipp, P.S., 2015,
847 Fault growth and interactions in a multiphase rift fault network: Horda Platform,
848 Norwegian North Sea: Journal of Structural Geology, v. 80, p. 99–119,
849 doi:10.1016/j.jsg.2015.08.015.
850 DuRoss, C.B., Personius, S.F., Crone, A.J., Olig, S.S., Hylland, M.D., Lund, W.R.,
851 and Schwartz, D.P., 2016, Fault segmentation: New concepts from the Wasatch
852 Fault Zone, Utah, USA: Journal of Geophysical Research: Solid Earth, v. 121, p.
853 1131–1157, doi:10.1002/2015JB012519.
854 Ebinger, C., 2005, Continental break-up: The East African perspective: Astronomy
855 and Geophysics, v. 46, p. 2.16-2.21, doi:10.1111/j.1468-4004.2005.46216.x.
856 Ebinger, C.J., 1989, Geometric and kinematic development of border faults and
857 accommodation zones, Kivu-Rusizi Rift, Africa: Tectonics, v. 8, p. 117–133,
858 doi:10.1029/TC008i001p00117.
859 Ebinger, C., Djomani, Y.P., Mbede, E., Foster, A., and Dawson, J.B., 1997, Rifting
860 Archaean lithosphere: the Eyasi-Manyara-Natron rifts, East Africa: Journal of the
861 Geological Society, v. 154, p. 947–960, doi:10.1144/gsjgs.154.6.0947.
862 Ebinger, C.J., Karner, G.D., and Weissel, J.K., 1991, Mechanical strength of
863 extended continental lithosphere: Constraints from the Western Rift System,
864 East Africa: Tectonics, v. 10, p. 1239–1256, doi:10.1029/91TC00579.
865 Eby, G.N., Roden-Tice, M., Krueger, H.L., Ewing, W., Faxon, E.H., and Woolley,
866 A.R., 1995, Geochronology and cooling history of the northern part of the Chilwa
867 Alkaline Province, Malawi: Journal of African Earth Sciences, v. 20, p. 275–288,
868 doi:10.1016/0899-5362(95)00054-W.
869 Fagereng, Å., 2013, Fault segmentation, deep rift earthquakes and crustal rheology:

Insights from the 2009 Karonga sequence and seismicity in the Rukwa-Malawi rift zone: Tectonophysics, v. 601, p. 216–225, doi:10.1016/j.tecto.2013.05.012.

Field, E.H. et al., 2009, Uniform California Earthquake Rupture Forecast, Version 2 (UCERF 2): Bulletin of the Seismological Society of America, v. 99, p. 2053–2107, doi:10.1785/0120080049.

Fliervoet, T.F., White, S.H., and Drury, M.R., 1997, Evidence for dominant grain-boundary sliding deformation in greenschist- and amphibolite-grade polymineralic ultramylonites from the Redbank Deformed Zone, Central Australia: Journal of Structural Geology, v. 19, p. 1495–1520, doi:10.1016/S0191-8141(97)00076-X.

Fossen, H., and Rotevatn, A., 2016, Fault linkage and relay structures in extensional settings-A review: Earth-Science Reviews, v. 154, p. 14–28, doi:10.1016/j.earscirev.2015.11.014.

Fullgraf, T., Dombola, K., Hyvonen, E., Thomas, B., and Zammit, C. The Provisional GEMMAP 1:1 Million Scale structural and geological maps of Malawi: Geological Survey of Malawi,.

Gaherty, J.B. et al., 2019, Faulting processes during early-stage rifting: Seismic and geodetic analysis of the 2009-2010 Northern Malawi earthquake sequence: Geophysical Journal International, v. 217, p. 1767–1782, doi:10.1093/gji/ggz119.

Gawthorpe, R.L., Jackson, C.A.-L., Young, M.J., Sharp, I.R., Moustafa, A.R., and Leppard, C.W., 2003, Normal fault growth, displacement localisation and the evolution of normal fault populations: the Hammam Faraun fault block, Suez rift, Egypt: Journal of Structural Geology, v. 25, p. 883–895, doi:10.1016/S0191-8141(02)00088-3.

895 Gawthorpe, R.L., and Leeder, M.R., 2000, Tectono-sedimentary evolution of active
896 extensional basins: Basin Research, v. 12, p. 195–218, doi:10.1111/j.1365-
897 2117.2000.00121.x.
898 Giba, M., Walsh, J.J., and Nicol, A., 2012, Segmentation and growth of an obliquely
899 reactivated normal fault: Journal of Structural Geology, v. 39, p. 253–267,
900 doi:10.1016/j.jsg.2012.01.004.
901 Goodwin, L.B., and Tikoff, B., 2002, Competency contrast, kinematics, and the
902 development of foliations and lineations in the crust: Journal of Structural
903 Geology, v. 24, p. 1065–1085, doi:10.1016/S0191-8141(01)00092-X.
904 Graymer, R.W., Langenheim, V.E., Simpson, R.W., Jachens, R.C., and Ponce, D.A.,
905 2007, Relatively simple through-going fault planes at large-earthquake depth
906 may be concealed by the surface complexity of strike-slip faults: Geological
907 Society, London, Special Publications, v. 290, p. 189–201,
908 doi:10.1144/SP290.5.
909 Gupta, A., and Scholz, C.H., 2000, A model of normal fault interaction based on
910 observations and theory: Journal of Structural Geology, v. 22, p. 865–879,
911 doi:10.1016/S0191-8141(00)00011-0.
912 Habgood, F., 1963, The geology of the country west of the Shire River between
913 Chikwawa and Chiromo: Bulletin of the Geological Survey, Malawi, v. 14.
914 Habgood, F., Holt, D.N., and Walshaw, R.D., 1973, The geology of the Thyolo Area:
915 Bulletin of the Geological Survey, Malawi, v. 22.
916 Hamling, I.J. et al., 2017, Complex multifault rupture during the 2016 Mw 7.8
917 Kaikōura earthquake, New Zealand: Science, v. 356,
918 doi:10.1126/science.aam7194.
919 Handy, M.R., 1990, The solid-state flow of polymineralic rocks: Journal of

Geophysical Research, v. 95, p. 8647, doi:10.1029/JB095iB06p08647.

Healy, D., Rizzo, R.E., Cornwell, D.G., Farrell, N.J.C., Watkins, H., Timms, N.E., Gomez-Rivas, E., and Smith, M., 2017, FracPaQ: A MATLAB™ toolbox for the quantification of fracture patterns: Journal of Structural Geology, v. 95, p. 1–16, doi:10.1016/j.jsg.2016.12.003.

Heermance, R., Shipton, Z.K., and Evans, J.P., 2003, Fault structure control on fault slip and ground motion during the 1999 rupture of the Chelungpu fault, Taiwan: Bulletin of the Seismological Society of America, v. 93, p. 1034–1050, doi:10.1785/0120010230.

Heilman, E., Kolawole, F., Atekwana, E.A., and Mayle, M., 2019, Controls of Basement Fabric on the Linkage of Rift Segments: Tectonics, v. 38, p. 1337–1366, doi:10.1029/2018TC005362.

Hellebrekers, N., Niemeijer, A.R., Fagereng, Å., Manda, B., and Mvula, R.L.S., 2019, Lower crustal earthquakes in the East African Rift System: Insights from frictional properties of rock samples from the Malawi rift: Tectonophysics, v. 767, p. 228167, doi:10.1016/j.tecto.2019.228167.

Henstra, G.A., Rotevatn, A., Gawthorpe, R.L., and Ravnås, R., 2015, Evolution of a major segmented normal fault during multiphase rifting: The origin of plan-view zigzag geometry: Journal of Structural Geology, v. 74, p. 45–63, doi:10.1016/j.jsg.2015.02.005.

Henza, A.A., Withjack, M.O., and Schlische, R.W., 2011, How do the properties of a pre-existing normal-fault population influence fault development during a subsequent phase of extension? Journal of Structural Geology, v. 33, p. 1312–1324, doi:10.1016/j.jsg.2011.06.010.

Hodge, M., Biggs, J., Fagereng, Å., Elliott, A., Mdala, H., and Mphepo, F., 2019, A

945 semi-automated algorithm to quantify scarp morphology (SPARTA): Application
946 to normal faults in southern Malawi: Solid Earth, v. 10, p. 27–57, doi:10.5194/se-
947 10-27-2019.
948 Hodge, M., Fagereng, and Biggs, J., 2018a, The Role of Coseismic Coulomb Stress
949 Changes in Shaping the Hard Link Between Normal Fault Segments: Journal of
950 Geophysical Research: Solid Earth, v. 123, p. 797–814,
951 doi:10.1002/2017JB014927.
952 Hodge, M., Fagereng, Biggs, J., and Mdala, H., 2018b, Controls on Early-Rift
953 Geometry: New Perspectives From the Bilila-Mtakataka Fault, Malawi:
954 Geophysical Research Letters, v. 45, p. 3896–3905,
955 doi:10.1029/2018GL077343.
956 Holdsworth, R.E., Butler, C.A., and Roberts, A.M., 1997, The recognition of
957 reactivation during continental deformation: Journal of the Geological Society, v.
958 154, p. 73–78, doi:10.1144/gsjgs.154.1.0073.
959 Hollinsworth, A.D., Koehn, D., Dempster, T.J., and Aanyu, K., 2019, Structural
960 controls on the interaction between basin fluids and a rift flank fault: Constraints
961 from the Bwamba Fault, East African Rift: Journal of Structural Geology, v. 118,
962 p. 236–249, doi:10.1016/j.jsg.2018.10.012.
963 Johnson, K., Nissen, E., Saripalli, S., Arrowsmith, J.R., McGarey, P., Scharer, K.,
964 Williams, P., and Blisniuk, K., 2014, Rapid mapping of ultrafine fault zone
965 topography with structure from motion: Geosphere, v. 10, p. 969–986,
966 doi:10.1130/GES01017.1.
967 Johnson, S.P., Rivers, T., and De Waele, B., 2005, A review of the Mesoproterozoic
968 to early Palaeozoic magmatic and tectonothermal history of south–central
969 Africa: implications for Rodinia and Gondwana: Journal of the Geological

970 Society, v. 162, p. 433–450, doi:10.1144/0016-764904-028.
971 Karmakar, S., and Schenk, V., 2016, Mesoproterozoic UHT metamorphism in the
972 Southern Irumide Belt, Chipata, Zambia: Petrology and in situ monazite dating:
973 Precambrian Research, v. 275, p. 332–356,
974 doi:10.1016/j.precamres.2016.01.018.
975 Katumwehe, A.B., Abdelsalam, M.G., and Atekwana, E.A., 2015, The role of pre-
976 existing Precambrian structures in rift evolution: The Albertine and Rhino
977 grabens, Uganda: Tectonophysics, v. 646, p. 117–129,
978 doi:10.1016/j.tecto.2015.01.022.
979 Kinabo, B.D., Atekwana, E.A., Hogan, J.P., Modisi, M.P., Wheaton, D.D., and
980 Kampunzu, A.B., 2007, Early structural development of the Okavango rift zone,
981 NW Botswana: Journal of African Earth Sciences, v. 48, p. 125–136,
982 doi:10.1016/j.jafrearsci.2007.02.005.
983 Kinabo, B.D., Hogan, J.P., Atekwana, E.A., Abdelsalam, M.G., and Modisi, M.P.,
984 2008, Fault growth and propagation during incipient continental rifting: Insight
985 from a combined aeromagnetic and Shuttle Radar Topography Mission digital
986 elevation model investigation of the Okavango Rift Zone, northwest Botswana:
987 Tectonics, v. 27, p. 1–16, doi:10.1029/2007TC002154.
988 Kirkpatrick, J.D., Bezerra, F.H.R., Shipton, Z.K., Do Nascimento, A.F., Pytharouli,
989 S.I., Lunn, R.J., and Soden, A.M., 2013, Scale-dependent influence of pre-
990 existing basement shear zones on rift faulting: A case study from NE Brazil:
991 Journal of the Geological Society, v. 170, p. 237–247, doi:10.1144/jgs2012-043.
992 Kristensen, T.B., Rotevatn, A., Peacock, D.C.P., Henstra, G.A., Midtkandal, I., and
993 Grundvåg, S.A., 2016, Structure and flow properties of syn-rift border faults: The
994 interplay between fault damage and fault-related chemical alteration (Dombjerg

995 Fault, Wollaston Forland, NE Greenland): Journal of Structural Geology, v. 92,
996 p. 99–115, doi:10.1016/j.jsg.2016.09.012.
997 Kröner, A., Willner, A.P., Hegner, E., Jaeckel, P., and Nemchin, A., 2001, Single
998 zircon ages, PT evolution and Nd isotopic systematics of high-grade gneisses in
999 southern Malawi and their bearing on the evolution of the Mozambique belt in
1000 southeastern Africa: Precambrian Research, v. 109, p. 257–291,
1001 doi:10.1016/S0301-9268(01)00150-4.
1002 Laõ-Dávila, D.A., Al-Salmi, H.S., Abdelsalam, M.G., and Atekwana, E.A., 2015,
1003 Hierarchical segmentation of the Malawi Rift: The influence of inherited
1004 lithospheric heterogeneity and kinematics in the evolution of continental rifts:
1005 Tectonics, v. 34, p. 2399–2417, doi:10.1002/2015TC003953.
1006 Lavayssière, A., Drooff, C., Ebinger, C., Gallacher, R., Illsley-Kemp, F., Oliva, S.J.,
1007 and Keir, D., 2019, Depth Extent and Kinematics of Faulting in the Southern
1008 Tanganyika Rift, Africa: Tectonics, v. 38, p. 842–862,
1009 doi:10.1029/2018TC005379.
1010 Leeder, M.R., and Gawthorpe, R.L., 1987, Sedimentary models for extensional tilt-
1011 block/half-graben basins: Geological Society, London, Special Publications, v.
1012 28, p. 139–152, doi:10.1144/GSL.SP.1987.028.01.11.
1013 Lettis, W., Bachhuber, J., Witter, R., Brankman, C., Randolph, C.E., Barka, A., Page,
1014 W.D., and Kaya, A., 2002, Influence of Releasing Step-Overs on Surface Fault
1015 Rupture and Fault Segmentation: Examples from the 17 August 1999 Izmit
1016 Earthquake on the North Anatolian Fault, Turkey: Bulletin of the Seismological
1017 Society of America, v. 92, p. 19–42, doi:10.1785/0120000808.
1018 Macdonald, R., Crossley, R., and Waterhouse, K.S., 1983, Karroo basalts of
1019 southern Malawi and their regional petrogenetic significance: Mineralogical

1020 Magazine, v. 47, p. 281–289, doi:10.1180/minmag.1983.047.344.02.
1021 Macey, P.H. et al., 2010, Mesoproterozoic geology of the Nampula Block, northern
1022 Mozambique: Tracing fragments of Mesoproterozoic crust in the heart of
1023 Gondwana: Precambrian Research, v. 182, p. 124–148,
1024 doi:10.1016/j.precamres.2010.07.005.
1025 Machette, M.N., Personius, S.F., Nelson, A.R., Schwartz, D.P., and Lund, W.R.,
1026 1991, The Wasatch fault zone, utah—segmentation and history of Holocene
1027 earthquakes: Journal of Structural Geology, v. 13, p. 137–149,
1028 doi:10.1016/0191-8141(91)90062-N.
1029 Manda, B.W.C., Cawood, P.A., Spencer, C.J., Prave, T., Robinson, R., and Roberts,
1030 N.M.W., 2019, Evolution of the Mozambique Belt in Malawi constrained by
1031 granitoid U-Pb, Sm-Nd and Lu-Hf isotopic data: Gondwana Research, v. 68, p.
1032 93–107, doi:10.1016/j.gr.2018.11.004.
1033 McConnell, R.B., 1967, The East African Rift System: Nature, v. 215, p. 578–581,
1034 doi:10.1038/215578a0.
1035 Mitchell, T.M., and Faulkner, D.R., 2009, The nature and origin of off-fault damage
1036 surrounding strike-slip fault zones with a wide range of displacements: A field
1037 study from the Atacama fault system, northern Chile: Journal of Structural
1038 Geology, v. 31, p. 802–816, doi:10.1016/j.jsg.2009.05.002.
1039 Montési, L.G.J., 2013, Fabric development as the key for forming ductile shear
1040 zones and enabling plate tectonics: Journal of Structural Geology, v. 50, p. 254–
1041 266, doi:10.1016/j.jsg.2012.12.011.
1042 Morewood, N.C., and Roberts, G.P., 2000, The geometry, kinematics and rates of
1043 deformation within an en echelon normal fault segment boundary, central Italy:
1044 Journal of Structural Geology, v. 22, p. 1027–1047, doi:10.1016/S0191-

8141(00)00030-4.

Morley, C.K., 2010, Stress re-orientation along zones of weak fabrics in rifts: An explanation for pure extension in ‘oblique’ rift segments? Earth and Planetary Science Letters, v. 297, p. 667–673, doi:10.1016/j.epsl.2010.07.022.

Mortimer, E., Kirstein, L.A., Stuart, F.M., and Strecker, M.R., 2016, Spatio-temporal trends in normal-fault segmentation recorded by low-temperature thermochronology: Livingstone fault scarp, Malawi Rift, East African Rift System: Earth and Planetary Science Letters, v. 455, p. 62–72, doi:10.1016/j.epsl.2016.08.040.

Mortimer, E., Paton, D.A., Scholz, C.A., Strecker, M.R., and Blisniuk, P., 2007, Orthogonal to oblique rifting: effect of rift basin orientation in the evolution of the North basin, Malawi Rift, East Africa: Basin Research, v. 19, p. 393–407, doi:10.1111/j.1365-2117.2007.00332.x.

Muirhead, J.D., and Kattenhorn, S.A., 2018, Activation of preexisting transverse structures in an evolving magmatic rift in East Africa: Journal of Structural Geology, v. 106, p. 1–18, doi:10.1016/j.jsg.2017.11.004.

Muirhead, J.D., Wright, L.J.M., and Scholz, C.A., 2019, Rift evolution in regions of low magma input in East Africa: Earth and Planetary Science Letters, v. 506, p. 332–346, doi:10.1016/j.epsl.2018.11.004.

Nicol, A., Childs, C., Walsh, J.J., Manzocchi, T., and Schöpfer, M.P.J., 2017, Interactions and growth of faults in an outcrop-scale system: Geological Society, London, Special Publications, v. 439, p. 23–39, doi:10.1144/SP439.9.

Nicol, A., Walsh, J., Berryman, K., and Nodder, S., 2005, Growth of a normal fault by the accumulation of slip over millions of years: Journal of Structural Geology, v. 27, p. 327–342, doi:10.1016/j.jsg.2004.09.002.

1070 Ord, D.M., Clemmey, H., and Leeder, M.R., 1988, Interaction between faulting and
1071 sedimentation during Dinantian extension of the Solway basin, SW Scotland:
1072 Journal - Geological Society (London), v. 145, p. 249–259,
1073 doi:10.1144/gsjgs.145.2.0249.
1074 Peacock, D.C.., and Sanderson, D.., 1991, Displacements, segment linkage and
1075 relay ramps in normal fault zones: Journal of Structural Geology, v. 13, p. 721–
1076 733, doi:10.1016/0191-8141(91)90033-F.
1077 Petersen, M.D. et al., 2015, The 2014 United States National Seismic Hazard Model:
1078 Earthquake Spectra, v. 31, p. S1–S30, doi:10.1193/120814EQS210M.
1079 Philippon, M., Willingshofer, E., Sokoutis, D., Corti, G., Sani, F., Bonini, M., and
1080 Cloetingh, S., 2015, Slip re-orientation in oblique rifts: Geology, v. 43, p. 147–
1081 150, doi:10.1130/G36208.1.
1082 Poirier, J.P., 1980, Shear localization and shear instability in materials in the ductile
1083 field: Journal of Structural Geology, v. 2, p. 135–142, doi:10.1016/0191-
1084 8141(80)90043-7.
1085 Prater, W.T. et al., 2016, Strain Accomodation of Cenezoic Rifting in the Northern
1086 Margin of the Shire Graben, Southern Malawi Rift: American Geophysical Union,
1087 Fall Meeting Abstracts,.
1088 Roberts, E.M., Stevens, N.J., O'Connor, P.M., Dirks, P.H.G.M., Gottfried, M.D.,
1089 Clyde, W.C., Armstrong, R.A., Kemp, A.I.S., and Hemming, S., 2012, Initiation
1090 of the western branch of the East African Rift coeval with the eastern branch:
1091 Nature Geoscience, v. 5, p. 289–294, doi:10.1038/ngeo1432.
1092 Robertson, E.A.M., Biggs, J., Cashman, K. V., Floyd, M.A., and Vye-Brown, C.,
1093 2016, Influence of regional tectonics and pre-existing structures on the formation
1094 of elliptical calderas in the Kenyan Rift: Geological Society Special Publication,

v. 420, p. 43–67, doi:10.1144/SP420.12.

Rotevatn, A., Jackson, C.A.L., Tvedt, A.B.M., Bell, R.E., and Blækkan, I., 2019, How do normal faults grow? Journal of Structural Geology, v. 125, p. 174–184, doi:10.1016/j.jsg.2018.08.005.

Rotevatn, A., Kristensen, T.B., Ksienzyk, A.K., Wemmer, K., Henstra, G.A., Midtkandal, I., Grundvåg, S.A., and Andresen, A., 2018, Structural Inheritance and Rapid Rift-Length Establishment in a Multiphase Rift: The East Greenland Rift System and its Caledonian Orogenic Ancestry: Tectonics, v. 37, p. 1858–1875, doi:10.1029/2018TC005018.

Samsu, A., Cruden, A.R., Micklethwaite, S., Grose, L., and Vollgger, S.A., 2020, Scale matters: The influence of structural inheritance on fracture patterns: Journal of Structural Geology, v. 130, p. 103896, doi:10.1016/j.jsg.2019.103896.

Savage, H.M., and Brodsky, E.E., 2011, Collateral damage: Evolution with displacement of fracture distribution and secondary fault strands in fault damage zones: Journal of Geophysical Research, v. 116, p. B03405, doi:10.1029/2010JB007665.

Schlische, R.W., Young, S.S., Ackermann, R. V., and Gupta, A., 1996, Geometry and scaling relations of a population of very small rift-related normal faults: Geology, v. 24, p. 683–686, doi:10.1130/0091-7613(1996)024<0683:GASROA>2.3.CO;2.

Scholz, C.H., Dawers, N.H., Yu, J.Z., Anders, M.H., and Cowie, P.A., 1993, Fault growth and fault scaling laws: preliminary results: Journal of Geophysical Research, v. 98, p. 951–961.

Segall, P., and Pollard, D.D., 1980, Mechanics of discontinuous faults: Journal of Geophysical Research: Solid Earth, v. 85, p. 4337–4350,

1120 doi:10.1029/JB085iB08p04337.
1121 Senger, K., Buckley, S.J., Chevallier, L., Fagereng, Å., Galland, O., Kurz, T.H.,
1122 Ogata, K., Planke, S., and Tveranger, J., 2015, Fracturing of doleritic intrusions
1123 and associated contact zones: Implications for fluid flow in volcanic basins:
1124 Journal of African Earth Sciences, v. 102, p. 70–85,
1125 doi:10.1016/j.jafrearsci.2014.10.019.
1126 Shipton, Z.K., and Cowie, P.A., 2003, A conceptual model for the origin of fault
1127 damage zone structures in high-porosity sandstone: Journal of Structural
1128 Geology, v. 25, p. 333–344, doi:10.1016/S0191-8141(02)00037-8.
1129 Shipton, Z.K., and Cowie, P.A., 2001, Damage zone and slip-surface evolution over
1130 μm to km scales in high-porosity Navajo sandstone, Utah: Journal of Structural
1131 Geology, v. 23, p. 1825–1844, doi:10.1016/S0191-8141(01)00035-9.
1132 Smith, M., and Mosley, P., 1993, Crustal heterogeneity and basement influence on
1133 the development of the Kenya Rift, East Africa: Tectonics, v. 12, p. 591–606,
1134 doi:10.1029/92TC01710.
1135 Stamps, D.S., Saria, E., and Kreemer, C., 2018, A Geodetic Strain Rate Model for
1136 the East African Rift System: Scientific Reports, v. 8, p. 1–8,
1137 doi:10.1038/s41598-017-19097-w.
1138 Stenvall, C.A., Fagereng, Å., and Diener, J.F.A., 2019, Weaker Than Weakest: On
1139 the Strength of Shear Zones: Geophysical Research Letters, v. 46, p. 7404–
1140 7413, doi:10.1029/2019GL083388.
1141 Tenthorey, E., and Cox, S.F., 2006, Cohesive strengthening of fault zones during the
1142 interseismic period: An experimental study: Journal of Geophysical Research:
1143 Solid Earth, v. 111, p. 1–14, doi:10.1029/2005JB004122.
1144 Terzaghi, R.D., 1965, Sources of Error in Joint Surveys: Géotechnique, v. 15, p.

287–304, doi:10.1680/geot.1965.15.3.287.

Torabi, A., and Berg, S.S., 2011, Scaling of fault attributes: A review: Marine and Petroleum Geology, v. 28, p. 1444–1460, doi:10.1016/j.marpetgeo.2011.04.003.

Torabi, A., Johannessen, M.U., and Ellingsen, T.S.S., 2019, Fault Core Thickness: Insights from Siliciclastic and Carbonate Rocks: Geofluids, v. 2019, p. 1–24, doi:10.1155/2019/2918673.

Turcotte, D.L., and Schubert, G., 2002, Geodynamics: New York, Cambridge University Press, 607 p.

Valentini, A., Duross, C.B., Field, E.H., Gold, R.D., Briggs, R.W., Visini, F., and Pace, B., 2019, Relaxing Segmentation on the Wasatch Fault Zone : Impact on Seismic Hazard: v. XX, doi:10.1785/0120190088.

Walker, R.T., Wegmann, K.W., Bayasgalan, A., Carson, R.J., Elliott, J., Fox, M., Nissen, E., Sloan, R.A., Williams, J.M., and Wright, E., 2017, The Egiin Davaa prehistoric rupture, central Mongolia: a large magnitude normal faulting earthquake on a reactivated fault with little cumulative slip located in a slowly deforming intraplate setting: Geological Society, London, Special Publications, v. 432, p. 187–212, doi:10.1144/SP432.4.

Walsh, J.J., Bailey, W.R., Childs, C., Nicol, A., and Bonson, C.G., 2003, Formation of segmented normal faults: A 3-D perspective: Journal of Structural Geology, v. 25, p. 1251–1262, doi:10.1016/S0191-8141(02)00161-X.

Walsh, J.J., Nicol, A., and Childs, C., 2002, An alternative model for the growth of faults: Journal of Structural Geology, v. 24, p. 1669–1675, doi:10.1016/S0191-8141(01)00165-1.

Walters, R.J. et al., 2018, Dual control of fault intersections on stop-start rupture in the 2016 Central Italy seismic sequence: Earth and Planetary Science Letters,

v. 500, p. 1–14, doi:10.1016/j.epsl.2018.07.043.

Wästeby, N., Skelton, A., Tollefsen, E., Andrén, M., Stockmann, G., Claesson Liljedahl, L., Sturkell, E., and Mörth, M., 2014, Hydrochemical monitoring, petrological observation, and geochemical modeling of fault healing after an earthquake: Journal of Geophysical Research: Solid Earth, v. 119, p. 5727–5740, doi:10.1002/2013JB010715.

Watterson, J., 1975, Mechanism for the persistence of tectonic lineaments: Nature, v. 253, p. 520–522, doi:10.1038/253520b0.

Wedmore, L.N.J., Biggs, J., Williams, J.N., Fagereng, Å., Dulanya, Z., Mphepo, F., and Mdala, H., 2019, Active fault scarps in southern Malawi and their implications for the distributino and evolution of strain in amagmatic continental rifts: EarthArXiv, doi:10.31223/osf.io/ujchx.

Wei, S. et al., 2011, Superficial simplicity of the 2010 El Mayor–Cucapah earthquake of Baja California in Mexico: Nature Geoscience, v. 4, p. 615–618, doi:10.1038/ngeo1213.

Wesnousky, S.G., 2008, Displacement and geometrical characteristics of earthquake surface ruptures: Issues and implications for seismic-hazard analysis and the process of earthquake rupture: Bulletin of the Seismological Society of America, v. 98, p. 1609–1632, doi:10.1785/0120070111.

Wesnousky, S.G., 2006, Predicting the endpoints of earthquake ruptures: Nature, v. 444, p. 358–360, doi:10.1038/nature05275.

Westerhof, A.P., Lehtonen, M.I., Mäkitie, H., Manninen, T., Pekkala, Y., Gustafsson, B., and Tahon, A., 2008, The Tete-Chipata Belt: a new multiple terrane element from western Mozambique and southern Zambia: Geological Survey of Finland Special PAper, v. 48, p. 145–166.

1195 Wheeler, W.H., and Karson, J.A., 1989, Structure and kinematics of the Livingstone
1196 Mountains border fault zone, Nyasa (Malawi) Rift, southwestern Tanzania:
1197 Journal of African Earth Sciences (and the Middle East), v. 8, p. 393–413,
1198 doi:10.1016/S0899-5362(89)80034-X.
1199 Whipp, P.S., Jackson, C.A.L., Gawthorpe, R.L., Dreyer, T., and Quinn, D., 2014,
1200 Normal fault array evolution above a reactivated rift fabric; a subsurface
1201 example from the northern Horda Platform, Norwegian North Sea: Basin
1202 Research, v. 26, p. 523–549, doi:10.1111/bre.12050.
1203 Willemse, E.J.M., 1997, Segmented normal faults: Correspondence between three-
1204 dimensional mechanical models and field data: Journal of Geophysical
1205 Research: Solid Earth, v. 102, p. 675–692, doi:10.1029/96jb01651.
1206 Willemse, E.J.M., Pollard, D.D., and Aydin, A., 1996, Three-dimensional analyses of
1207 slip distributions on normal fault arrays with consequences for fault scaling:
1208 Journal of Structural Geology, v. 18, p. 295–309, doi:10.1016/S0191-
1209 8141(96)80051-4.
1210 Williams, J.N., Fagereng, Å., Wedmore, L.N.J., Biggs, J., Mphepo, F., Dulanya, Z.,
1211 Mdala, H., and Blenkinsop, T., 2019, How Do Variably Striking Faults Reactivate
1212 During Rifting? Insights From Southern Malawi: Geochemistry, Geophysics,
1213 Geosystems, p. 3588–3607, doi:10.1029/2019gc008219.
1214 Williams, J.N., Toy, V.G., Smith, S.A.F., and Boulton, C., 2017, Fracturing, fluid-rock
1215 interaction and mineralisation during the seismic cycle along the Alpine Fault:
1216 Journal of Structural Geology, v. 103, p. 151–166,
1217 doi:10.1016/j.jsg.2017.09.011.
1218 Wilson, J.., Chester, J.., and Chester, F.., 2003, Microfracture analysis of fault
1219 growth and wear processes, Punchbowl Fault, San Andreas system, California:

Journal of Structural Geology, v. 25, p. 1855–1873, doi:10.1016/S0191-8141(03)00036-1.

Woolley, A.R., 1987, Lithosphere metasomatism and the petrogenesis of the Chilwa Province of alkaline igneous rocks and carbonatites, Malawi: Journal of African Earth Sciences, v. 6, p. 891–898, doi:10.1016/0899-5362(87)90048-0.

Woolley, A.R., Bevan, J.C., and Elliott, C.J., 1979, The Karroo dolerites of southern Malawi and their regional geochemical implications: Mineralogical Magazine, v. 43, p. 487–495, doi:10.1180/minmag.1979.043.328.08.

Worthington, R.P., and Walsh, J.J., 2017, Timing, growth and structure of a reactivated basin-bounding fault: Geological Society, London, Special Publications, v. 439, p. 511–531, doi:10.1144/SP439.14.

Zangerl, C., Loew, S., and Eberhardt, E., 2006, Structure, geometry and formation of brittle discontinuities in anisotropic crystalline rocks of the Central Gotthard Massif, Switzerland: Eclogae Geologicae Helvetiae, v. 99, p. 271–290, doi:10.1007/s00015-006-1190-0.

Zeeb, C., Gomez-Rivas, E., Bons, P.D., and Blum, P., 2013, Evaluation of sampling methods for fracture network characterization using outcrops: AAPG Bulletin, v. 97, p. 1545–1566, doi:10.1306/02131312042.

Zhang, P., Slemmons, D.B., and Mao, F., 1991, Geometric pattern, rupture termination and fault segmentation of the Dixie Valley-Pleasant Valley active normal fault system, Nevada, U.S.A.: Journal of Structural Geology, v. 13, p. 165–176, doi:10.1016/0191-8141(91)90064-P.

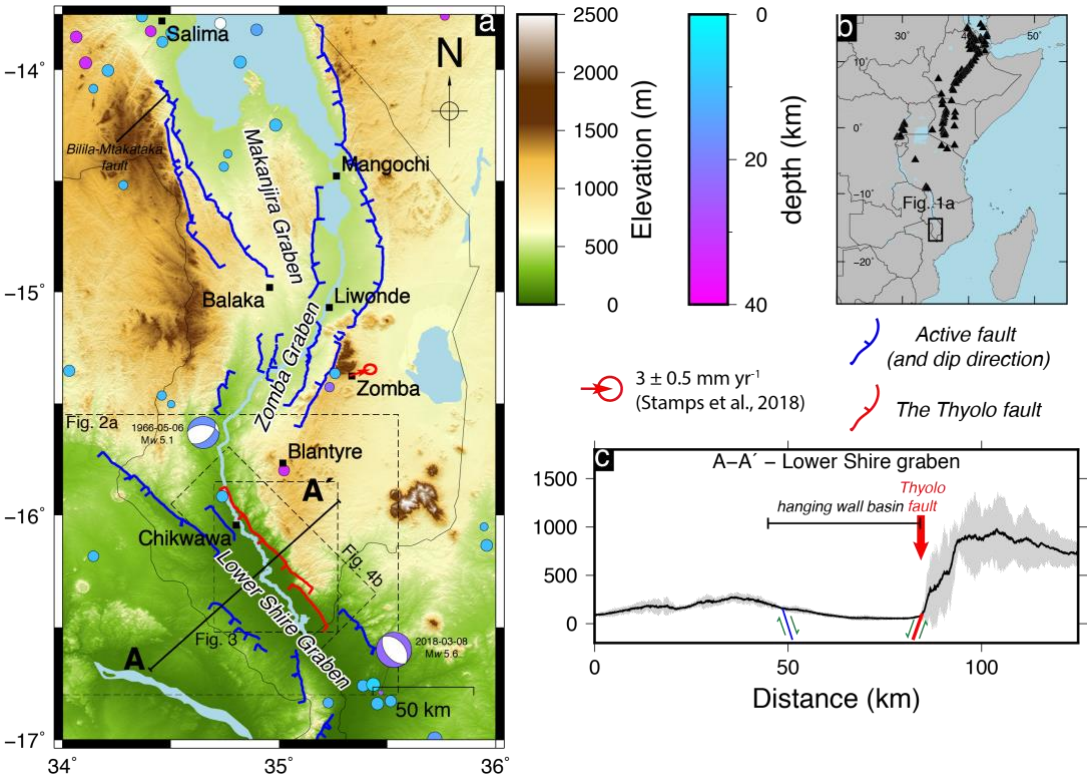

1243 Figure 1. The location and tectonic context of the Lower Shire Graben. (a) The
1244 southern Malawi rift system with known active fault scarps in blue and the Thyolo
1245 fault highlighted in red. Also shown is the GPS vector from a station in Zomba,
1246 National Earthquake Information Centre earthquake locations from 1971-2018
1247 (circles coloured by depth), and focal mechanisms for the two largest events in the
1248 region, a M_w5.1 earthquake in 1966 (from Craig et al., 2011) and the CMT solution
1249 for the 2018 Nsanje earthquake (M_w5.6). (b) The location of the southern Malawi rift
1250 system within the East African Rift. Triangles indicate Holocene active volcanoes. (c)
1251 Swath topographic cross section across the Lower Shire Graben extracted from
1252 TanDEM-X data. Black line is the median elevation with the grey shading the
1253 maximum and minimum elevation 10 km either side of profile A-A` indicated in part
1254 a.
1255

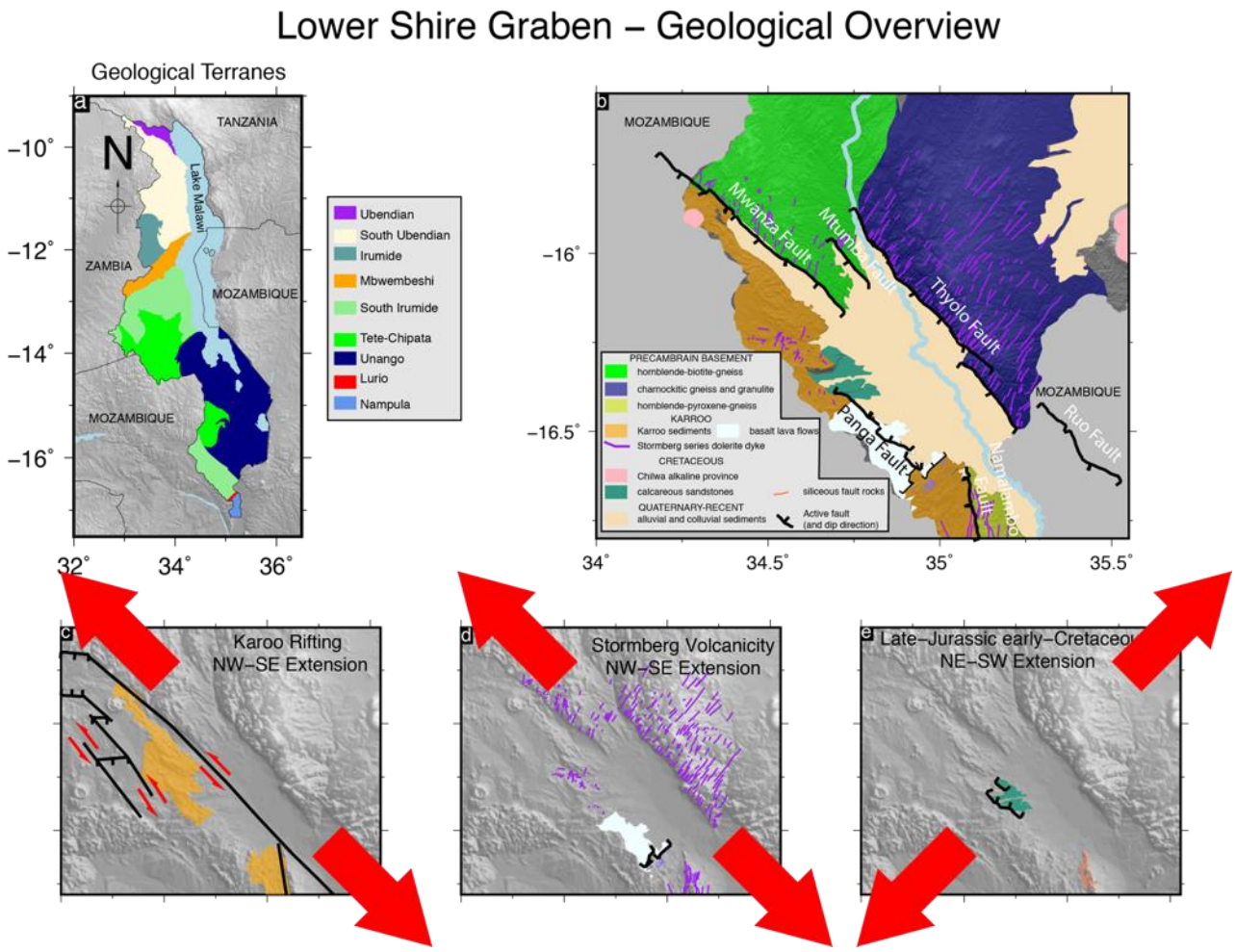

Figure 2. Geological overview of the Lower Shire Graben. (a) Geological terranes within Malawi (Fullgraf et al., *in press*). (b) Simplified geological map of the Lower Shire Graben adapted from Hapgood 1963. (c) Structures related to NW-SE amagmatic extension during the Karoo period. (d) Dykes and normal faults associated with NW-SE magmatic rifting in the late Karoo period. (e) Normal faults and sedimentary deposits related to NE-SW rifting during the Late-Jurassic to early-Cretaceous.

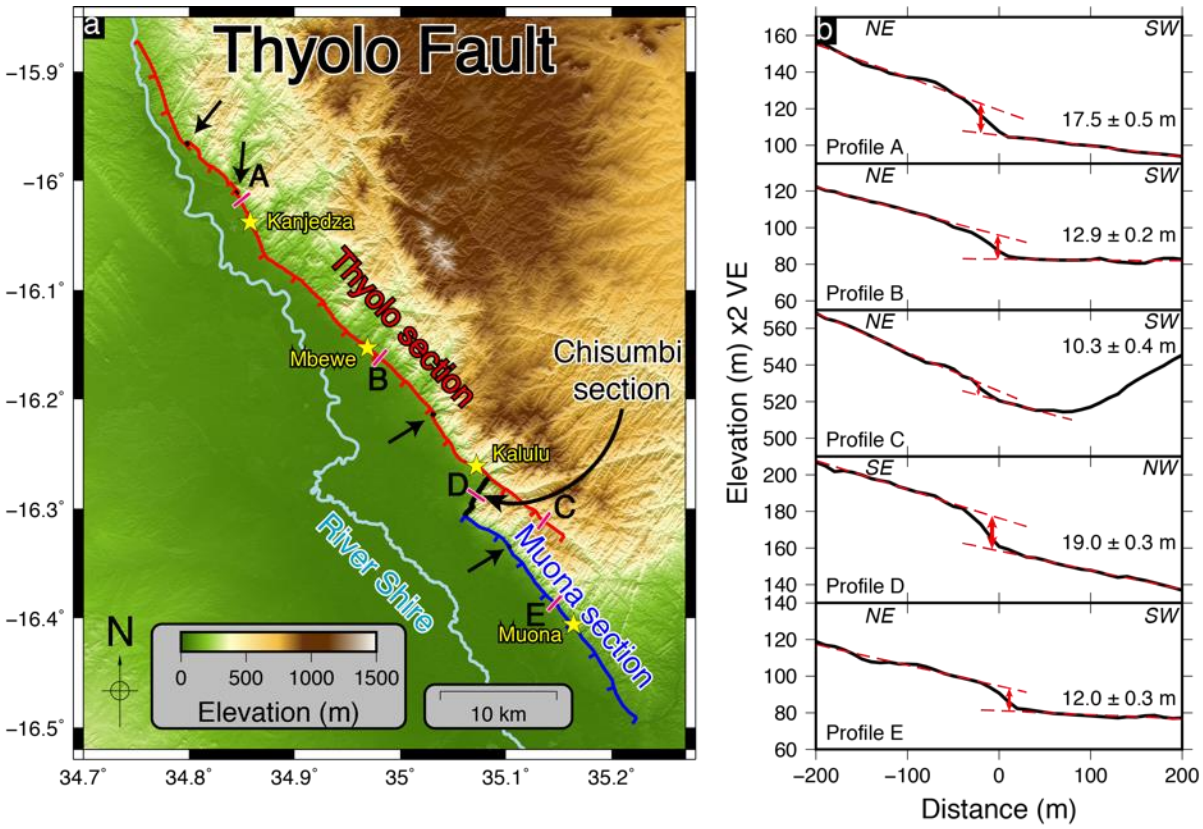

Figure 3 (a) TanDEM-X digital elevation model of the Thyolo fault showing both the Thyolo (red) and Muona (blue) sections. The fault sections oriented at ~90° to the main strike are indicated in black with sections visible at this scale identified by black arrows . Yellow stars indicate the locations of field studies reported in this paper. Pink rectangles indicate are the locations and orientation of illustrative topographic profiles extracted perpendicular to the fault scarp and shown in part b. (b) Example topographic profiles extracted perpendicular the fault scarp. All profiles are plotted with the footwall on the left-hand side (profile orientation is indicated in the top left). Note profile D is located along the Chisumbi section where the strike is oriented ~90° to the strike of the main fault sections.

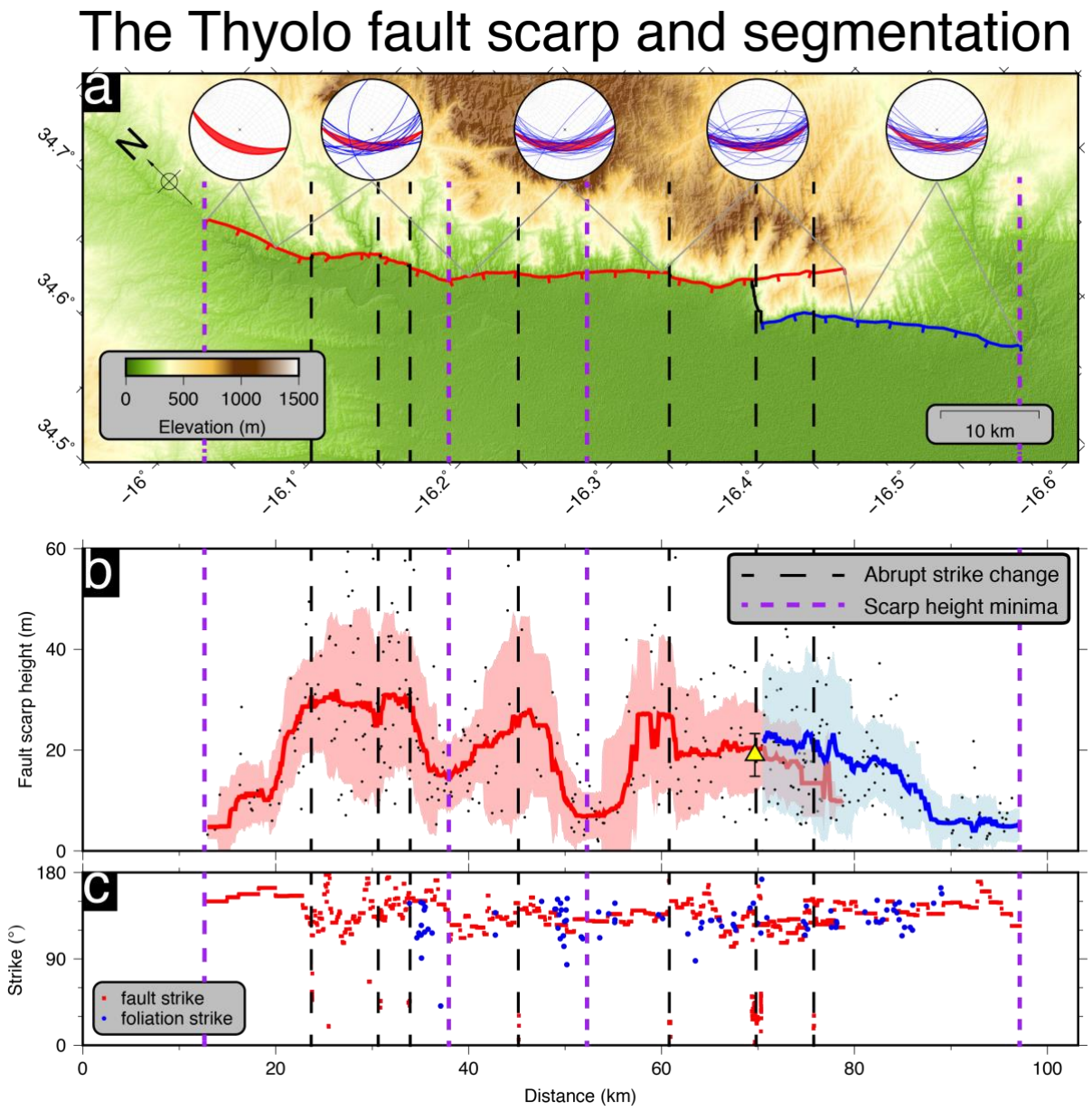

Figure 4. Thyolo fault scarp height and segmentation. (a) A rotated view of the Thyolo fault showing different indicators of fault segmentation. Inset equal angle, lower hemisphere stereonets are rotated into the same view as the underlying map. Red ellipses shows the mean fault orientation measured every 20 km, with a dip value plotted between 45°-60°, and the blue lines show foliation orientations. (b) The height of the Thyolo fault scarp as a function of distance from the NW to the SE along the fault. (c) The strike of the Thyolo fault (measured every 50 m) and foliation strike measurements (Habgood et al., 1973) as a function of distance from NW to SE

along the fault. Scarp height in b was measured using topographic profiles, perpendicular to the scarp, extracted every 100 m along strike. Black dots are the individual measurements with the solid coloured lines the 5 km moving median of these measurements. The shaded areas represents the 1σ error bars. Red line is the Thyolo section, blue line is the Muona section. The yellow triangle (with 1σ error bars) is the scarp height along the ~4 km linking segment.

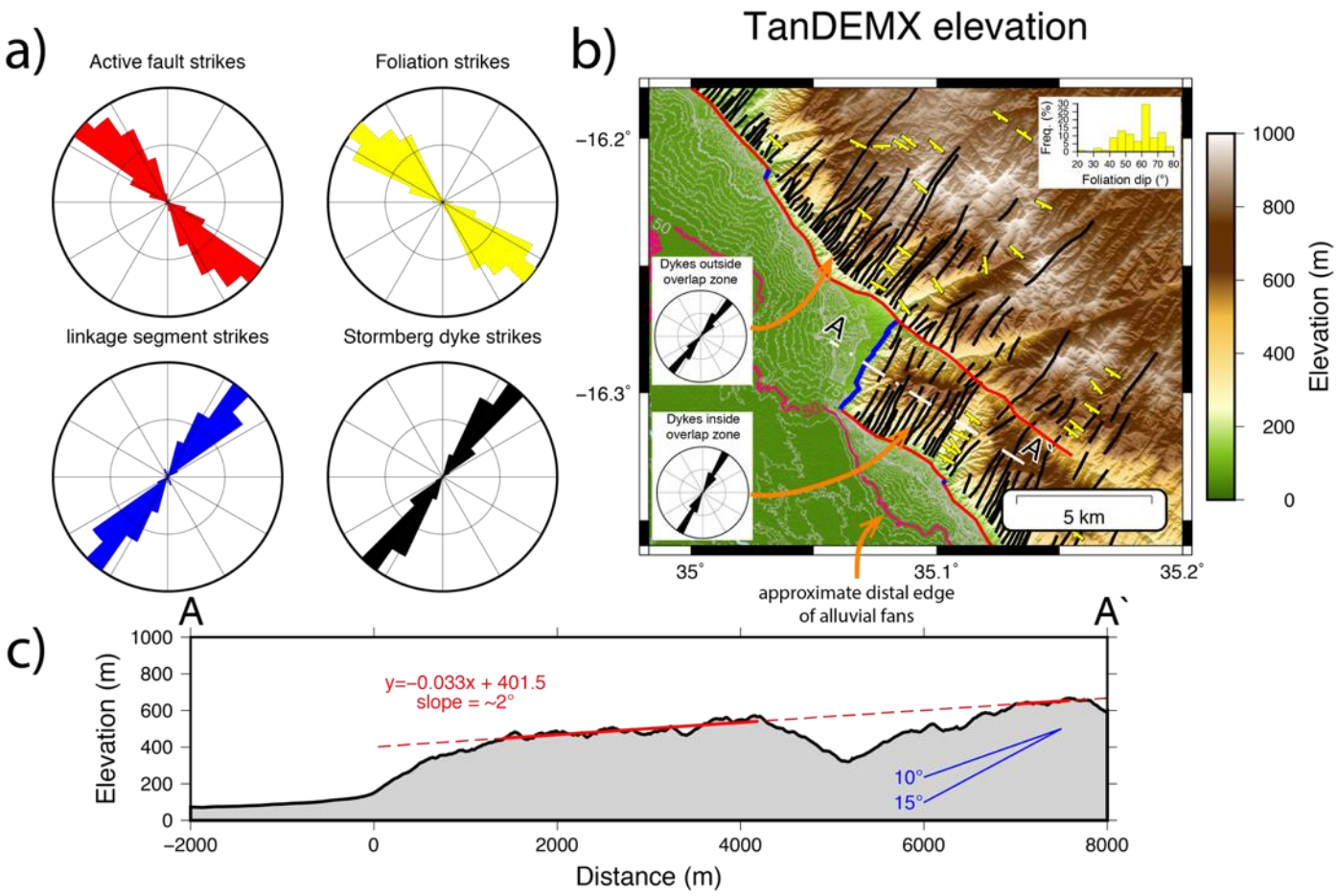

Figure 5. The linkage section between the Thyolo and Muona sections. (a) Rose diagrams of the orientation of surface traces of the different structures along the Thyolo fault. Active faults include the Thyolo and Muona fault sections as indicated on the map. The fault sections and dykes were divided into 50 m long sections before calculating the strike of each section. Linkage segments only include the sections of fault that strike approximately perpendicular to the Thyolo and Muona sections. Foliation orientations and Stormberg dykes were digitised from Habgood et al. (1973). (b) TanDEM-X DEM of the Chisumbi linkage section between the Thyolo and Muona sections. Dykes are indicated with black lines, foliation orientation and dip direction with yellow lines and ticks, faults with red lines and sections of the fault that strike perpendicular to the main fault with blue lines. Grey contour lines are 2.5 m apart, with the 50 m contour, which marks the approximate distal edge of alluvial fan complexes originating from footwall catchments, marked in pink. The inset

1304 histogram shows the dip of foliation measurements (Habgood et al., 1973). The inset
1305 rose diagrams show the orientation of dykes located inside and outside of the zone
1306 where the Thyolo and Muona sections overlap. (c) Swath topographic extracted
1307 along the transect A-A` shown in part b. The mean topography 1 km either side of
1308 the transect is plotted. The red line is a linear best fit to the slope of the topography
1309 within the portions of the solid red line. The dashed portions are not used as they
1310 have been affected by erosion due to river incision or include the fault scarp and fault
1311 facet slope. Angles which are the normal range of breached relay ramp dips
1312 (according to Fossen and Rotevatn, 2016) are plotted for comparison.
1313

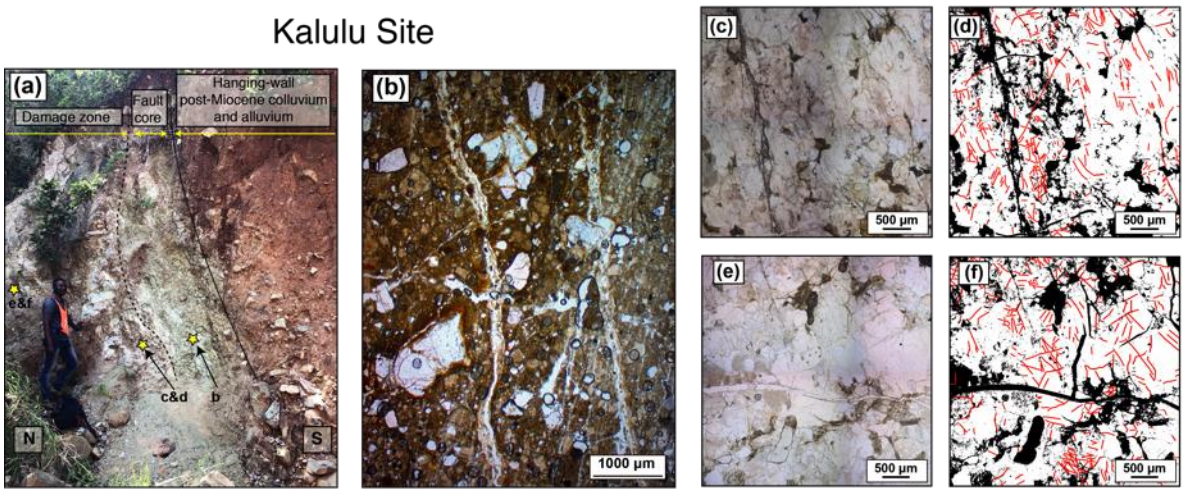

Figure 6 (a) Fault zone exposure at Kalulu showing juxtaposition of hanging wall sediments and footwall basement across a 0.7 m unit of fault gouge. Locations of samples used for photomicrographs in (b-f) shown by yellow stars. (b) photomicrograph of gouge with fractured quartz clasts and clay-rich brown matrix in plane polarised light (PPL) in sample from fault contact. (c-f) Photomicrographs of samples in PPL with adjacent image showing fracture traces (red lines) and areas (black) in sample not constituting quartz or feldspar grains that were omitted when calculating fracture density.

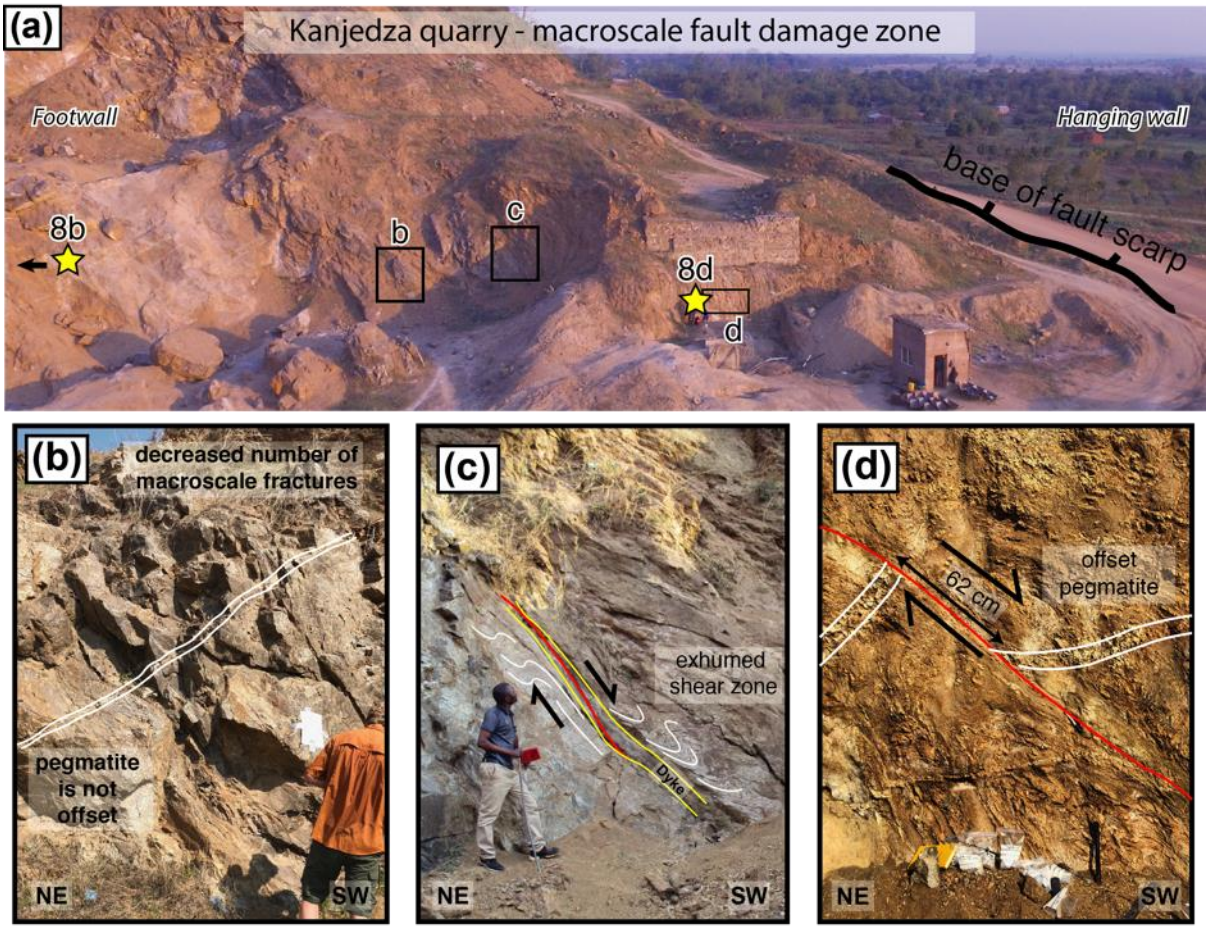

Figure 7. Macroscale fault damage zone at the Kanjedza site along the Thyolo fault. (a) A perspective view of the exposed fault zone indicating the location of sample macroscale photos shown in parts b-d. Locations of microscale observations shown in Figure 8 are indicated with yellow stars. (b) Outcrop from outside the macroscale fault damage zone, note the lack of fracturing within the basement rock when compared with c and d. (c) Outcrop within the fault damage zone showing an exhumed reverse sense shear zone and dyke. The dyke edge has been reactivated in a normal sense and acts as a minor slip surface. (d) Offset pegmatite within the footwall damage zone.

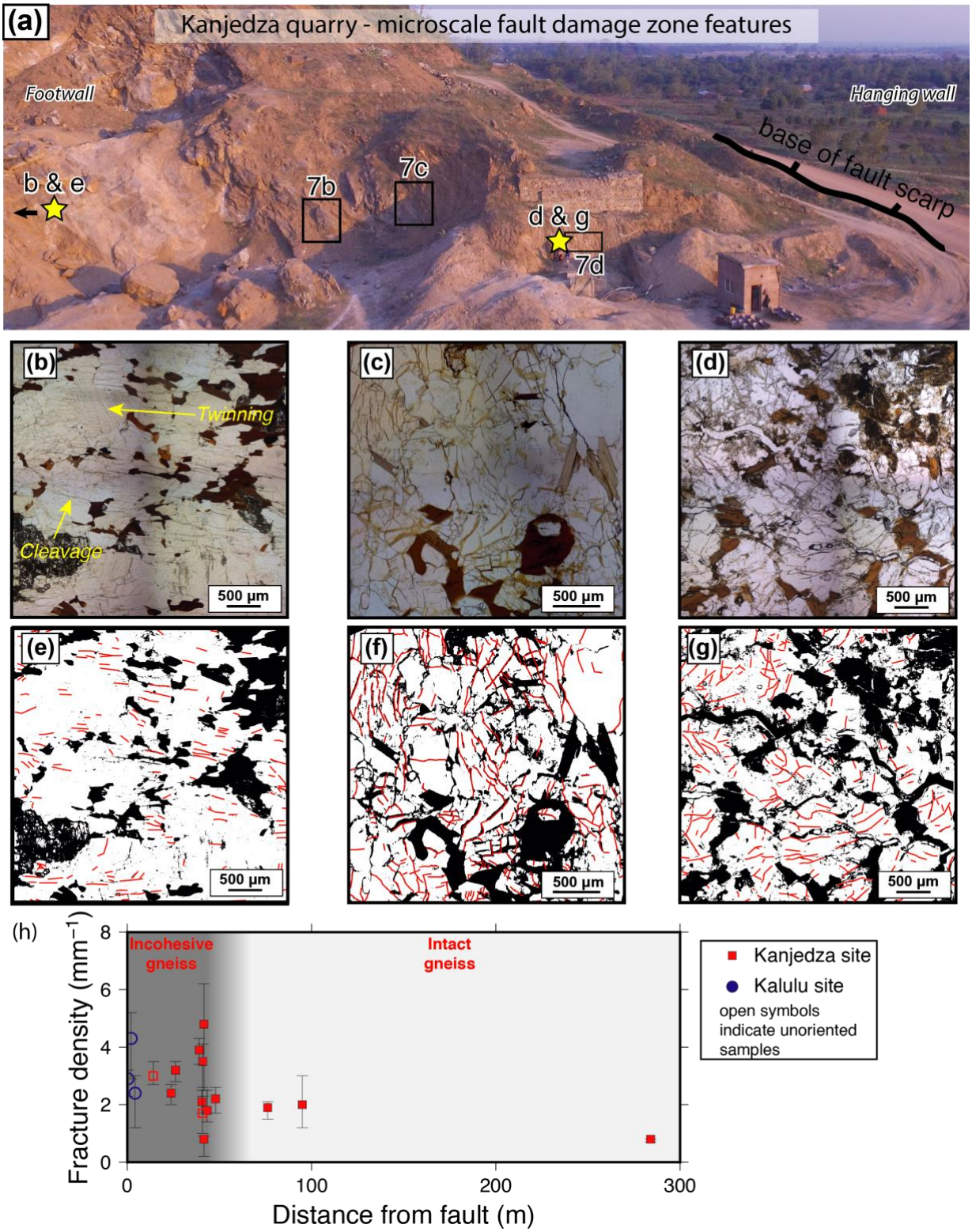

1337

1338 Figure 8. Microscale fault damage zone at Kanjedza Quarry. (a) An overview of the

1339 Kanjedza quarry fault zone exposure indicating the locations of the samples (yellow

1340 stars). (b) Photomicrograph of sample from outside the fault zone. (c)

Photomicrograph of a sample from a minor footwall slip surface. (d) Photomicrograph of a sample in the fault damage zone surrounding minor footwall fault and dyke (e-f) annotated photomicrographs of parts b-g showing the fractures (red lines) identified in each sample. (h) Compilation of fracture density plotted against distance from the fault for the Kanjedza and Kalulu sites along the Thyolo fault. The division between intact and incohesive gneiss is based on field observations (Figure 7).

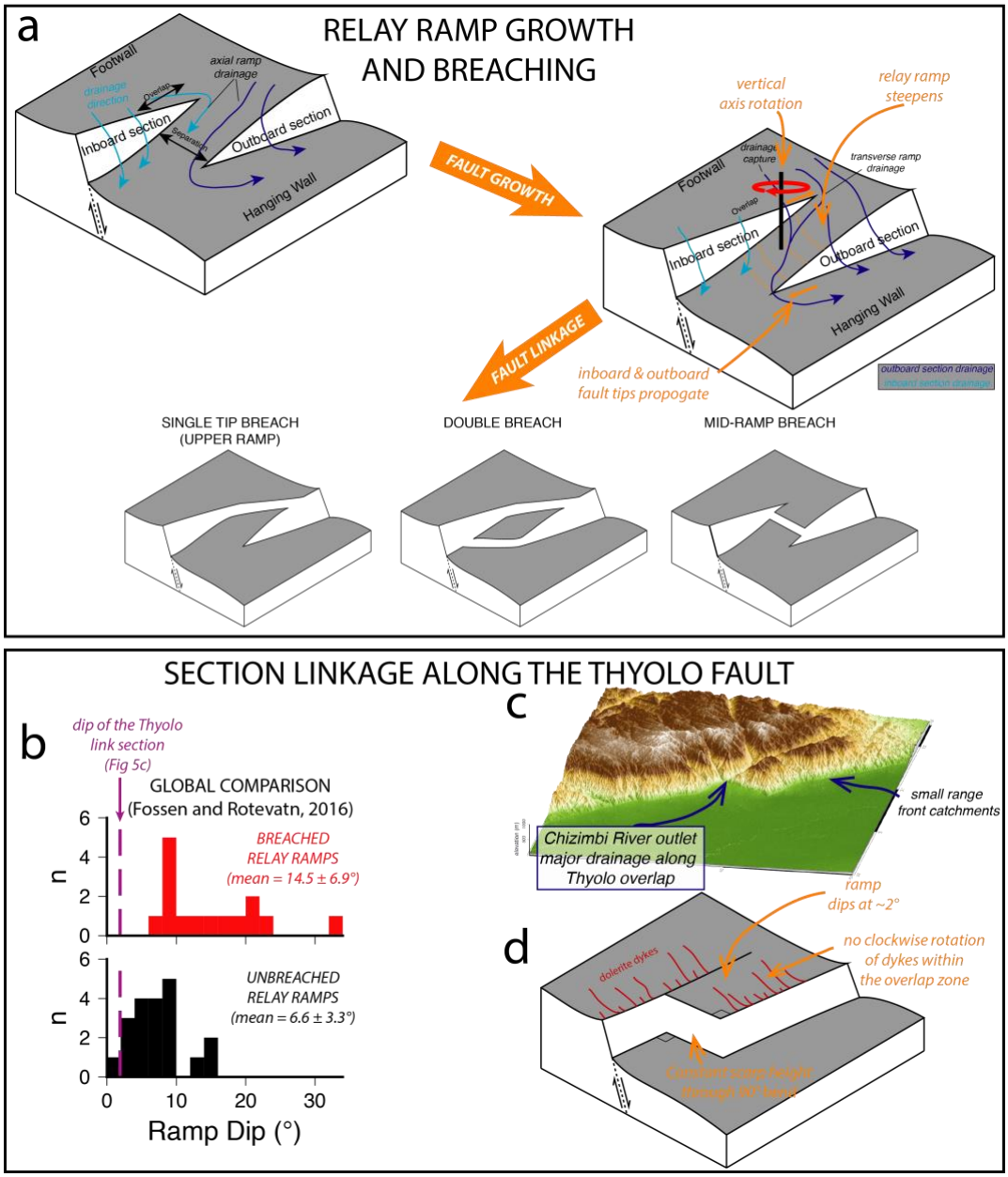

Figure 9. A comparison of relay ramp morphology and the linkage section between the Thyolo and Muona sections. (a) A summary of relay ramp growth and breaching (adapted from Fossen and Rotevatn, 2016). (b) The dip of relay ramp dips from a global compilation of breached and unbreached relay ramps (Fossen and Rotevatn, 2016). The dip of the topography in the section between the Thyolo and Muona sections is indicated with the purple dashed line. (c) A 3d view of the link section between the Thyolo and Muona sections showing the prominent drainage channels including the range front catchments that are predominate in the region and the

1358 triangular facets along the Chisumbi section. (d) A conceptual view of the way the

1359 Thyolo fault has linked between the Thyolo and Muona sections.

1360

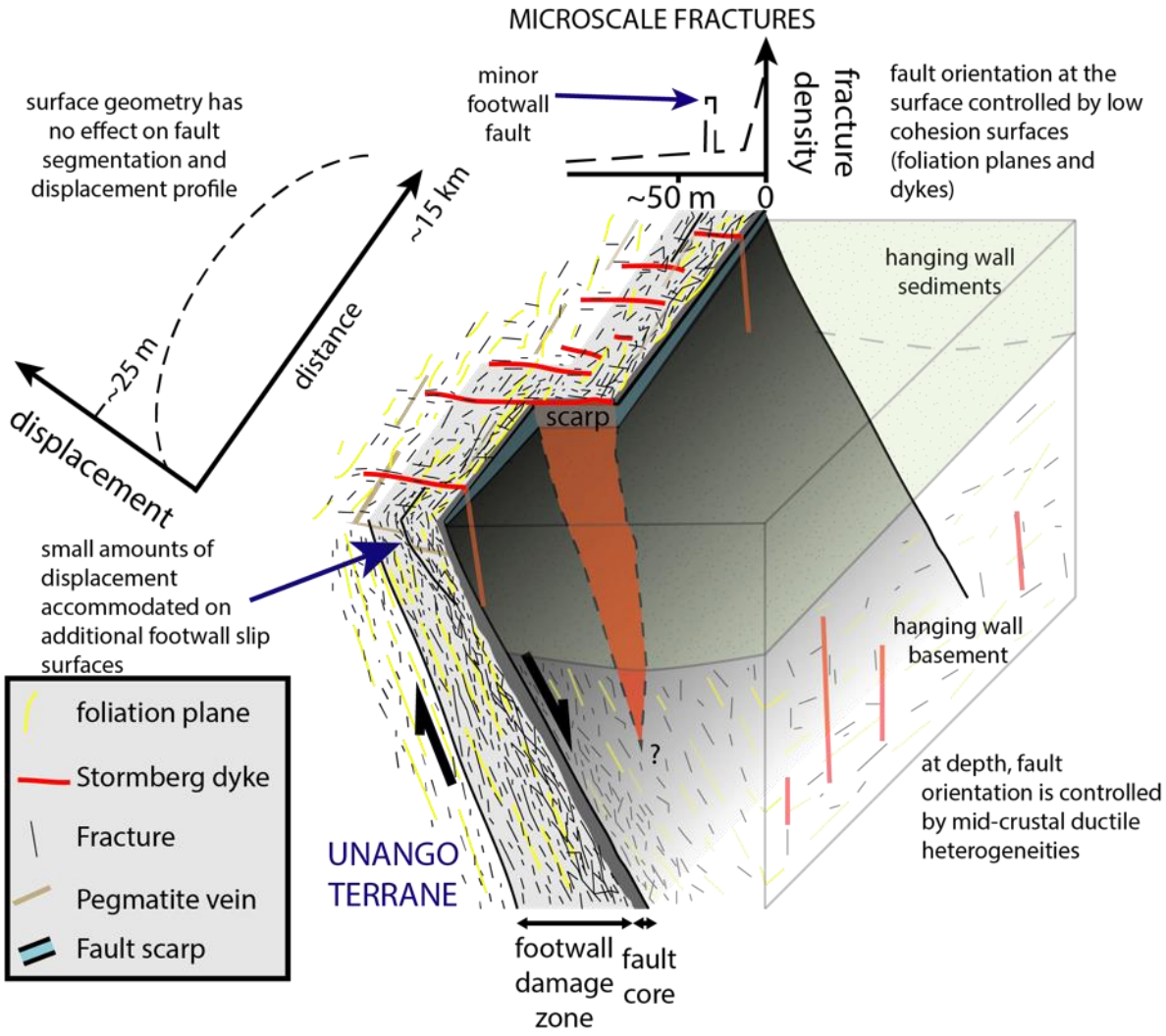

Figure 10. A conceptual model of the reactivation of the Thyolo fault towards the edge of the Unango Terrane boundary showing the relationship between shallow brittle structures which control the small scale surface geometry and fault damage zone structure, and deeper mid-crustal ductile, viscous structures associated with the terrane boundary which control the overall geometry of the fault and possibly the pattern of segmentation.